The dependence of aerosol effects on clouds and precipitation on cloud-system organization, shear and stability

Seoung Soo Lee,[1,2] Leo J. Donner,[1] Vaughan T. J. Phillips,[1,3] and Yi Ming[1]

Received 26 July 2007; revised 27 January 2008; accepted 27 March 2008; published 16 August 2008.

[1] Precipitation suppression due to an increase of aerosol number concentration in stratiform cloud is well-known. It is not certain whether the suppression applies for deep convection. Recent studies have suggested increasing precipitation from deep convection with increasing aerosols under some, but not all, conditions. Increasing precipitation with increasing aerosols can result from strong interactions in deep convection between dynamics and microphysics. High cloud liquid, due to delayed autoconversion, provides more evaporation, leading to more active downdrafts, convergence fields, condensation, collection of cloud liquid by precipitable hydrometeors, and precipitation. Evaporation of cloud liquid is a primary determinant of the intensity of the interactions. It is partly controlled by wind shear modulating the entrainment of dry air into clouds and transport of cloud liquid into unsaturated areas. Downdraft-induced convergence, crucial to the interaction, is weak for shallow clouds, generally associated with low convective available potential energy (CAPE). Aerosol effects on cloud and precipitation can vary with CAPE and wind shear. Pairs of idealized numerical experiments for high and low aerosol cases were run for five different environmental conditions to investigate the dependence of aerosol effect on stability and wind shear. In the environment of high CAPE and strong wind shear, cumulonimbus- and cumulus-type clouds were dominant. Transport of cloud liquid to unsaturated areas was larger at high aerosol, leading to stronger downdrafts. Because of the large vertical extent of those clouds, strong downdrafts and convergence developed for strong interactions between dynamics and microphysics. These led to larger precipitation at high aerosol. Detrainment of cloud liquid and associated evaporation were less with lower CAPE and wind shear, where dynamically weaker clouds dominated. Transport of cloud liquid to unsaturated areas was not as active as in the environment of high CAPE and strong shear. Also, evaporatively driven differences in downdrafts at their level of initial descent were not magnified in clouds with shallow depth as much as in deep convective clouds as they accelerated to the surface over shorter distances. Hence the interaction between dynamics and microphysics was reduced, leading to precipitation suppression at high aerosol. These results demonstrate that increasing aerosol can either decrease or increase precipitation for an imposed large-scale environment supporting cloud development. The implications for larger-scale aspects of the hydrological cycle will require further study with larger-domain models and cumulus parameterizations with advanced microphysics.

Citation: Lee, S. S., L. J. Donner, V. T. J. Phillips, and Y. Ming (2008), The dependence of aerosol effects on clouds and precipitation on cloud-system organization, shear and stability, *J. Geophys. Res.*, *113*, D16202, doi:10.1029/2007JD009224.

1. Introduction

[2] Aerosol indirect effects posit possible links between aerosols and, thereby, cloud condensation nuclei (CCN), and their impact on clouds in terms of radiation and precipitation. Anthropogenic CCN may cause an increase of the cloud droplet number concentration (CDNC), and, at constant liquid water content (LWC), a decrease of the droplet size. These modifications of cloud microphysical properties promote an increase in cloud albedo [*Twomey*, 1977]. This is generally referred to as the first indirect effect of aerosol. Previous studies pointed out that a decrease of the droplet size is also likely to impact cloud precipitation [*Albrecht*, 1989; *Warner*, 1968; *Gunn and Phillips*, 1957]. The decrease of the droplet size can deter the conversion of the droplet to drizzle or rain and increase the amount of low-

[1]Geophysical Fluid Dynamics Laboratory, Princeton University, Princeton, New Jersey, USA.
[2]Now at Department of Atmospheric, Oceanic, and Space Sciences, University of Michigan, Ann Arbor, Michigan, USA.
[3]Now at Department of Meteorology, University of Hawaii, Manoa, Hawaii, USA.

0148-0227/08/2007JD009224

level cloudiness through a reduction in precipitation. This precipitation suppression is commonly referred to as the second indirect effect of aerosol and may substantially alter the water mass budget of clouds, and thus alter their persistence, albedo, and, perhaps climate. However, recent studies by *van den Heever et al.* [2006], *Khain et al.* [2005], and *Lynn et al.* [2005] showed increasing precipitation for deep convection, associated with increases of aerosol number concentration and, thereby, CCN. These results are contrary to precipitation suppression discussed in the earlier cited studies for stratiform clouds. *Khain et al.* [2005] found these increases of precipitation in two cases. Both cases were characterized by unstable environments which developed deep convection and led to the formation of squall lines. The numerical simulations of *van den Heever et al.* [2006] of the impact of Saharan dust on Florida convection showed invigoration of deep convective clouds with increased ice nuclei (IN) from the dust. *Lynn et al.* [2005] simulated a squall line off the west coast of Florida and found heavier precipitation with higher aerosols. *Lynn et al.* [2005] analyzed the reason for more precipitation with higher aerosol number concentration and found stronger low-level convergence around the surface, induced by greater evaporation, played an important role. *Khain et al.* [2005], *Lynn et al.* [2005], and *Lee et al.* [2008] showed that sharp reductions in autoconversion at high aerosol are compensated by increases in condensation of cloud liquid and its collection by snow, graupel and rain. Increased evaporation resulting from larger cloud liquid at high aerosol generated increased downdraft activity with converging outflows.

[3] The Texas and CCOPE cases simulated by *Khain and Pokrovsky* [2004], *Khain et al.* [2004], *Cui et al.* [2006], and *Phillips et al.* [2007b] showed much less precipitation at high aerosol, as did the Amazon case simulated by *Khain et al.* [2008]. In these cases, as in those discussed above, convection was vertically extensive, with cloud tops at 14 to 15 km, vertical velocities exceeding 20 m s^{-1}, and anvils of 100-km length in the Texas cases. *Khain et al.* [2008] identify humidity as a key control on the sign of the precipitation response to increasing aerosols. In this study, we examine the possibility that CAPE and wind shear may also be strong controls on the response of deep convection to increasing aerosol. Stronger updrafts can sustain hydrometeors to increase collisions [*Pruppacher and Klett*, 1978] and carry cloud liquid to heights large enough to accelerate downdrafts. Updraft strength is partly determined by CAPE, and a system with low CAPE cannot develop strong downdraft-driven density currents [*Weisman and Klemp*, 1982], limiting the development of new convection associated with convergence produced by the current. The vertical shear of the horizontal wind influences the entrainment of dry air into clouds and the transport of cloud liquid into unsaturated areas, closely linked to the intensity of evaporation, downdrafts and converging outflows. Shallow cumuli and stratocumuli with low CAPE, wind shear, and vertical velocities, cannot develop strong interactions between microphysics, convergence fields, and intense downdrafts (simulated by *Khain et al.* [2005], *Lynn et al.* [2005], and *Lee et al.* [2008]). Without these interactions, the primary effect of increased aerosols is to reduce autoconversion and subsequently precipitation. A transition apparently exists across CAPE and wind shear over which precipitation responds differently to aerosol number concentration.

[4] Study of aerosol effects on mesoscale cloud ensembles (MCEs), accounting for a large proportion of the Earth's precipitation and thus important from a climatological standpoint [*Houze*, 1993], is in its infancy. The aim of the present paper is to investigate the dependence of the role of aerosol in the development and precipitation of MCEs on environmental conditions, represented by CAPE and shear. Simulating mesoscale systems requires a larger model domain and longer time integration than for an isolated single cloud. Hence most mesoscale studies have adopted bulk schemes due to the low computational cost they require, while bin-resolving schemes have been mostly used for the simulation of an isolated cloud. Bin-resolving schemes are more comprehensive than bulk schemes, since they explicitly calculate the particle size distribution. However, the computational cost associated with bin schemes is significantly higher than bulk schemes. Also, there are still unresolved issues related to application of bin schemes to cloud-system resolving models (CSRMs) with coarser spatial resolutions used for mesoscale studies (e.g., droplet nucleation [cf. *Saleeby and Cotton*, 2004], and the impact of entrainment and mixing on cloud droplet spectra [cf. *Grabowski*, 2006]). Hence bulk microphysics schemes remain a viable approach for the simulation of mesoscale systems [*Morrison and Grabowski*, 2007]. This study adopts a CSRM coupled with bulk microphysics based on *Phillips et al.*'s [2007a] double-moment scheme which predicts number as well as mass of cloud particles, allowing their sizes to be predicted. This double-moment microphysics has 6 classes of water: water vapor, cloud liquid, rain, cloud ice, snow, and graupel. Evaporation, condensation, deposition, sublimation, melting, freezing, and collision-coalescence between hydrometeors are considered.

[5] The immediate radiative impact of clouds depends on the size as well as mass of their particles. Particle size also influences cloud lifetime and spatial extent through the preferential sedimentation of larger particles and through the coagulation of cloud particles to form precipitation. Hence modification of cloud particle size by changing aerosol properties is one of the most essential parts in the simulation of aerosol-cloud interactions. The numerical representation of nucleation is important for the simulation of aerosol-cloud interactions, since nucleation predominantly determines numbers of cloud particles and affects the sizes of cloud particles [*Lohmann et al.*, 1999]. Aerosol and cloud particle properties and supersaturation characterize the nucleation processes [*Pruppacher and Klett*, 1978]. However, most bulk models have used saturation adjustment schemes to diagnose initial formation of cloud mass with no consideration of aerosol and cloud particle properties or supersaturation. Recently, to consider supersaturation and aerosol content, a prognostic representation of nucleation has been developed for double-moment microphysics by using supersaturation prediction. Development has also been devoted in recent years toward parameterization of nucleation with explicit representation of aerosols. *Ming et al.* [2006], *Nenes and Seinfeld* [2003], and *Abdul-Razzak*

and Ghan [2000] developed parameterizations calculating CCN activation based on the Köhler theory. In their parameterization, aerosols can take any form of size distribution and chemical composition, enabling the consideration of spatiotemporally varying aerosol properties for droplet nucleation. The parameterization of *Lohmann and Diehl* [2006] took into account the dependence of ice nuclei (IN) activation on dust and black carbon (BC) aerosol mass for contact, immersion, and condensation-freezing activation of IN. For deposition nucleation, *Möhler et al.* [2006] developed a parameterization calculating the fraction of dust activated. Hence their schemes enable aerosol composition to determine ice nucleation. For simulations in this study, the nucleation schemes of Ming et al., Lohmann and Diehl, and Möhler et al. are used in conjunction with the supersaturation scheme of *Phillips et al.* [2007a]. This enables the prediction of cloud particle number and size by taking into account predicted aerosol properties.

[6] Several pairs of numerical experiments with different environmental conditions, characterized by CAPE and wind shear, are carried out to examine the dependence of the role of aerosol number in MCE on environmental conditions. *Bluestein* [1993] has related CAPE and wind shear to storm type. In this paper, we select five representative environmental conditions from his classification.

[7] 1. High CAPE and strong wind shear.

[8] 2. High CAPE and weak wind shear.

[9] 3. Moderate CAPE and weak wind shear.

[10] 4. Low CAPE and weak wind shear.

[11] 5. Very low CAPE, less than 500 J kg^{-1}, and weak wind shear, with vertical temperature profiles suitable for warm shallow clouds.

[12] Each environmental condition is generated by modifying observations from subcase A of the 1997 Atmospheric Radiation Measurement (ARM) program. The conditions are then applied to high and low aerosol concentrations to investigate the sensitivity of cloud development and precipitation to aerosol number. The five conditions produce a range of sensitivities to aerosols.

2. CSRM

2.1. Dynamics, Turbulence, and Radiation

[13] For numerical experiments, the Weather Research and Forecasting (WRF) model [*Michalakes et al.*, 2001] is used as a two-dimensional nonhydrostatic compressible model. The detailed equations of the dynamical core of WRF are described by *Klemp et al.* [2007].

[14] *Hong and Pan*'s [1996] scheme, which includes nongradient flux for heat and moisture and calculates vertical eddy diffusion, is used for the planetary boundary layer. For vertical diffusion in the free troposphere, the scheme of *Hong et al.* [2006], where diffusion is represented with an implicit local scheme based on the local Richardson number, is used. The version of WRF used in these experiments uses a turbulence kinetic energy (TKE) closure. Horizontal eddy diffusion is a function of TKE, following *Chen and Dudhia* [2000].

[15] For radiation, a simplified version of the GFDL radiation code is incorporated into WRF [*Freidenreich and Ramaswamy*, 1999; *Schwarzkopf and Ramaswamy*, 1999]. The radiative effects of cloud liquid, cloud ice, rain, snow, graupel, water vapor, CO_2, and O_3 are included. Effective sizes of cloud liquid and cloud ice are predicted using assumed size distributions. A generalized effective size of cloud ice is inferred from the mean size of the equivalent spherical diameter following *Phillips et al.* [2007a].

2.2. Double-Moment Microphysics

[16] To represent microphysical processes, the WRF is modified to use the double-moment bulk representation of *Phillips et al.* [2007a]. The size distribution of cloud liquid and cloud ice (x = c, i) obeys a gamma distribution:

$$n(D_x) = n_{x,0} D_x^{p_x} \exp[-\lambda_x D_x] \quad (1)$$

where D_x is the equivalent spherical diameter (m) and $n(D_x)dD_x$ is the number concentration (m^{-3}) of particles in the size range dD_x. Also, $\lambda_x(m^{-1})$ is the slope, $n_{x,0}$ is the intercept ($m^{-(4+px)}$), and p_x is the shape parameter of the distribution.

$$\lambda_x = \left(\frac{\Gamma(4+p_x)\rho_x \frac{\pi}{6} n_x}{\Gamma(1+p_x) q_x} \right)^{\frac{1}{3}} \text{ and } n_{x,0} = (n_x \rho_a) \lambda_x^{1+p_x} / \Gamma(1+p_x).$$

Here, Γ is the Gamma function, ρ_x and n_x are the particle bulk density (kg m^{-3}) and number mixing ratio (kg^{-1}) (particle number per unit air mass), respectively. For ice particles, a bulk density close to that of pure solid-column ice crystal is assumed (ρ_i = 900 kg m^{-3}) [*Young*, 1993]. The general conclusions obtained in this study also hold if different bulk density of ice particles is used. However, the shape dependence of ice crystals on temperature and humidity has not been taken into account, and this could alter riming in the calculations. p_i and p_c are set to unity and 3.5, respectively, based on field experiments described by *Phillips et al.* [2007a]. Further description of the bulk microphysics can be found in *Phillips et al.* [2007a].

2.3. Droplet Nucleation

[17] Droplet nucleation follows the nucleation parameterization of *Ming et al.* [2006]. In their parameterization, aerosol can take any form of size distribution and chemical composition. Critical supersaturation (S_c) and critical radius (r_c) are calculated considering aerosol chemical composition, based on the Köhler theory. For surface tension depression by dissolved organic substances, the measured suppression of *Facchini et al.* [1999] is used. Maximum supersaturation (S_{max}) of a closed adiabatic parcel is calculated based on the equation of supersaturation prediction from *Leaitch et al.* [1986] for primary nucleation, occurring in cloud-free air. The supersaturation in the parcel increases with increasing vertical positive velocity of updrafts and decreases with increasing condensation. When the increase exactly counterbalances the decrease, the supersaturation is at its equilibrium S_{max}. S_{max} is obtained by solving Leaitch et al.'s equation of supersaturation prediction numerically. S_{max} for secondary nucleation (in-cloud nucleation) is obtained from the linearized supersaturation scheme of *Phillips et al.* [2007a]. Aerosols, whose S_c is lower than S_{max}, are counted as nucleated droplets by the parameterization of *Ming et al.* [2006].

2.4. Ice Nucleation

[18] The parameterizations of *Lohmann and Diehl* [2006], taking into account the dependence of IN activation on dust and BC aerosol mass, are used for contact, immersion, and condensation-freezing activation of IN. For contact activation:

$$\frac{dN_{CNT}}{dt}\left(\mathrm{m^{-3}\ s^{-1}}\right) = m_{io} D_{ap} 4\pi r_{cm} N_{a,cnt} \frac{\rho_a n_c^2}{q_c} \tag{2}$$

where $\frac{dN_{CNT}}{dt}$ is the rate of ice-crystal number production via contact freezing, m_{io} (10^{-12} kg) is the original mass of a newly formed ice crystal, D_{ap} ($\mathrm{m^2\ s^{-1}}$) is the Brownian aerosol diffusivity, r_{cm} is volume-mean droplet radius, $N_{a,cnt}$ ($\mathrm{m^{-3}}$) is the number concentration of contact nuclei and n_c is the number mixing ratio of droplets. D_{ap} is given by

$$D_{ap} = \frac{kTC_c}{6\pi\eta r_m}$$

where k is the Boltzmann constant, T is the temperature, η is the viscosity of air $\{\eta = 10^{-5}(1.718 + 0.0049(\mathrm{T}-\mathrm{T_0}) - 1.2 \times 10^{-5}(\mathrm{T}-\mathrm{T_0})^2)$ in kg $\mathrm{m^{-1}\ s^{-1}}\}$, r_m is the aerosol mode radius, and C_c is the Cunningham correction factor$[C_c = 1 + 1.26(\frac{\lambda}{r_m})(\frac{p_0}{p})(\frac{T}{T_0})]$. The aerosol mode radius is taken to be 0.2 μm for dust and 0.1 μm for BC. λ is the molecular free path length of air ($\lambda = 0.066$ μm), p_0 and T_0 refer to standard pressure of 1013.25 hPa and freezing temperature of 273.16 K. $N_{a,cnt}$ is obtained from the number of aerosol particles consisting of BC and dust, multiplied by a temperature dependence of the individual species. This temperature dependence is based on Figure 1 by *Lohmann and Diehl* [2006]. Here, for dust, temperature dependence of montmorillonite is adopted [*Lohmann and Diehl*, 2006]. For immersion and condensation-freezing activation:

$$\frac{dN_{IMM}}{dt}\left(\mathrm{m^{-3}\ s^{-1}}\right) = N_{a,imm} \exp(T_0 - T)\frac{dT}{dt}\frac{\rho_a q_c}{\rho_c} \tag{3}$$

where $\frac{dN_{IMM}}{dt}$ is the rate of ice-crystal number production via immersion and condensation freezing, T_0 freezing temperature. $N_{a,imm}$ ($\mathrm{m^{-3}}$) is the number concentration of immersion and condensation nuclei calculated as the number of BC and dust aerosols, multiplied by a temperature dependence for immersion and condensation freezing in Figure 1 by *Lohmann and Diehl* [2006]. As for contact freezing, temperature dependence of montmorillonite is adopted for dust. For deposition nucleation, the parameterization of *Möhler et al.* [2006], calculating the fraction of dust activated, is implemented:

$$\frac{dN_{DEP}}{dt}\left(\mathrm{m^{-3}\ s^{-1}}\right) = N_{a,dep}(\exp[a(S_i - S_0)] - 1) \tag{4}$$

where $\frac{dN_{DEP}}{dt}$ is the rate of ice-crystal number production via depositional freezing, a and S_0 are nondimensional empirical constants determined by chamber experiments, which are dependent on aerosol properties. Here a and S_0 are set to 4.77 and 1.07, respectively, based on experiments for desert dust. $N_{a,dep}$ is the number concentration of deposition nuclei ($\mathrm{m^{-3}}$) calculated from predicted total dust mass. (4) is applied at temperatures colder than -40°C and restricted to $S_0 < S_i < 1.63 + 6.52 \times 10^{-3} \times (\mathrm{T}-\mathrm{T_0})$, corresponding to the measured saturation region of *Field et al.* [2006] where pure deposition nucleation occurs. The parameterization is limited to activating a maximum of 5% of the dust, following the measurements of *Field et al.* [2006]. As indicated by the experiments of *Field et al.* [2006], (4) is only valid at temperatures below -40°C. At temperatures warmer than -40°C, the parameterizations of *Meyers et al.* [1992] and *DeMott et al.* [2003], multiplied by a scaling factor to consider the dependence of IN activation on dust mass, are used. Those parameterizations are applied to grid points with no cloud liquid to ensure only deposition nucleation is calculated. It is limited to activating a maximum of 0.5% of the dust, since *Field et al.* [2006] found deposition nucleation did not activate more than 0.5% of the dust at temperatures warmer than -40°C. Details of those parameterizations can be found in Appendix A. A list of symbols is presented in Table 1.

2.5. Integration Design

[19] A mesoscale convective system is defined as a cloud system that occurs in connection with an ensemble of thunderstorms and produces precipitation area ~100 km or more in horizontal scale in at least one direction [*Houze*, 1993]. The horizontal model domain for the numerical experiments is 168 km and the vertical domain is 20 km to cover a mesoscale cloud system. The horizontal grid length is 2 km and the vertical grid length is 500 m. Arakawa C-grid staggering is used.

[20] Periodic boundary conditions are set on horizontal boundaries, and heat and moisture fluxes are prescribed at the surface. To prevent the reflection of gravity or sound waves from the model top, a damping layer of 5-km depth is applied from 15 km to model top with a strength of $\mathrm{k_0}$ $(\mathrm{z}-\mathrm{z_0})$, where $\mathrm{k_0} = 2 \times 10^{-6}\ \mathrm{m^{-1}}$ and $\mathrm{z_0}$ is 15 km.

[21] The time integration scheme for WRF is a third-order Runge-Kutta-based time-splitting technique using a time step of 10 s [*Wicker and Skamarock*, 2002]. There is a high time-resolution integration of acoustic waves in addition.

[22] The five pairs of experiments, lasting 1 d, adopt data sets generated from observed data in subcase A (13:30 UTC 29 June to 13:30 UTC 30 June 1997) of the ARM Program over central Oklahoma described by *Zhang and Lin* [1997] and *Zhang et al.* [2001]. The subcase A produced the largest precipitation rate among the 1997 IOP three subcases.

[23] Five different sets of initial soundings and mean advective tendencies are generated.

[24] They provide initial conditions and large-scale advection for potential temperature and specific humidity. The advective tendencies correspond to time tendencies, which are applied uniformly to the thermodynamic and vapor equations over the model domain to represent the effects of the domain-average flow on the development of the cloud system. Details of the prescription of observed advective tendencies and surface fluxes of heat and moisture to the model are discussed by *Donner et al.* [1999].

[25] Convection in the model is initiated by imposing perturbations on the initial water vapor mixing ratio at the first time step. The perturbations vary in the horizontal but are constant throughout the lowest 1.5 km in each column of the model. The perturbations are horizontally random,

Table 1. List of Symbols

Notation	Description	Value	Units
a	Empirical constant used in deposition nucleation	4.77	Nondimensional
C_c	Cunningham correction factor	Predicted	Nondimensional
D_{ap}	Brownian aerosol diffusivity	Predicted	$m^2\ s^{-1}$
D_c	Diameter of cloud liquid	Varies within the diameter range of a given size distribution	m
D_i	Equivalent spherical diameter of cloud ice	Varies within the diameter range of a given size distribution	m
$DU_{2.5}$	Mass concentration of dust with diameter less than 2.5 μm	Predicted	$kg\ m^{-3}$
$DU^*_{2.5}$	Reference dust mass concentration	1.1×10^{-10}	$kg\ m^{-3}$
k	Boltzmann constant	1.38×10^{-23}	$J\ K^{-1}$
k_0	Constant used to determine the strength of damping layer	2×10^{-6}	m^{-1}
Lx	Domain length	1.68×10^5	m
m_{io}	Original mass of a newly formed ice crystal	10^{-12}	kg
$N_{a,cnt}$	Number concentration of contact nuclei	Predicted	m^{-3}
$N_{a,dep}$	Number concentration of deposition nuclei	Predicted	m^{-3}
$N_{a,imm}$	number concentration of immersion and condensation nuclei	Predicted	m^{-3}
N_{CNT}	Cloud-ice number concentration produced by contact activation of IN	Predicted	m^{-3}
N_{DEP}	Cloud-ice number concentration produced by depositional activation of IN	Predicted	m^{-3}
N_{IN}	Cloud-ice number concentration	Predicted	m^{-3}
N_{IMM}	Cloud-ice number concentration produced by immersion and condensational activation of IN	Predicted	m^{-3}
n_c	Number mixing ratio of cloud liquid	Predicted	kg^{-1}
n_i	Number mixing ratio of cloud ice	Predicted	kg^{-1}
$n_{c,0}$	Intercept parameter of cloud liquid distribution	Predicted	$m^{-(4+p_c)}$
$n_{i,0}$	Intercept parameter of cloud ice distribution	Predicted	$m^{-(4+p_c)}$
P	Pressure	Predicted	Pa
p_c	Shape parameter of cloud liquid distribution	3.5	Nondimensional
p_i	Shape parameter of cloud ice distribution	1	Nondimensional
p_0	Reference pressure	1.01325×10^5	Pa
q_c	Mixing ratio of cloud liquid	Predicted	Nondimensional, $kg\ kg^{-1}$
q_g	Mixing ratio of graupel	Predicted	Nondimensional, $kg\ kg^{-1}$
q_i	Mixing ratio of cloud ice	Predicted	Nondimensional, $kg\ kg^{-1}$
q_r	Mixing ratio of rain	Predicted	Nondimensional, $kg\ kg^{-1}$
q_s	Mixing ratio of snow	Predicted	Nondimensional, $kg\ kg^{-1}$
q_v	Mixing ratio of water vapor	Predicted	Nondimensional, $kg\ kg^{-1}$
r_c	Critical radius of droplets for nucleation	Calculated based on Köhler theory	m
r_{cm}	Volume-mean droplet radius	Predicted	m
r_m	Aerosol mode radius	0.2×10^{-6} for dust 0.1×10^{-6} for BC	m
S_c	Critical supersaturation of droplets for nucleation	Calculated based on Köhler theory	Nondimensional
S_0	Empirical constant used in deposition nucleation	1.07	Nondimensional
S_i	Ice saturation ratio	Predicted	Nondimensional
S_{max}	Maximum parcel supersaturation	Predicted	Nondimensional
T	Temperature	Predicted	K
T_0	Freezing temperature	273.16	K
u	Horizontal velocity	Predicted	$m\ s^{-1}$
w	Vertical velocity	Predicted	$m\ s^{-1}$
w_{max}	Maximum cloud draft strength in a grid column	Predicted	$m\ s^{-1}$
z_0	Bottom level of damping layer	1.5×10^4	m
ρ_a	Air density	Predicted	$kg\ m^{-3}$
ρ_c	Bulk density of cloud liquid	1000	$kg\ m^{-3}$
ρ_i	Bulk density of cloud ice	900	$kg\ m^{-3}$
λ	Molecular free length of air	6.6×10^{-8}	m
λ_c	Slope parameter of cloud liquid distribution	Predicted	m^{-1}
η	Viscosity of air	Predicted	$kg\ m^{-1}\ s^{-1}$
Ψ	Scaling factor used in deposition nucleation	Predicted	Nondimensional

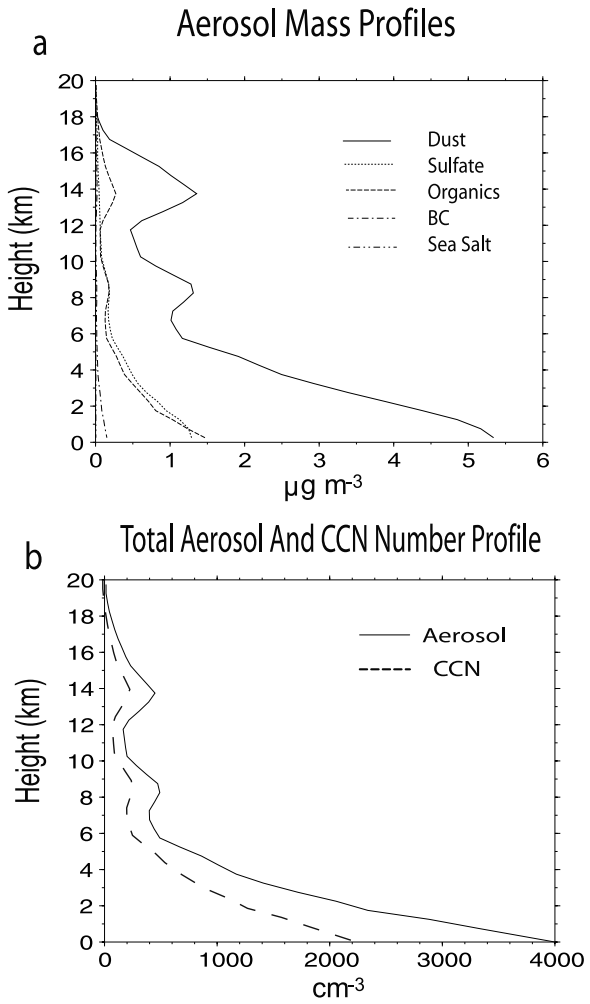

Figure 1. Vertical profiles of (a) aerosol species and (b) total aerosol number and CCN number (at supersaturation of 1%) for high aerosol runs. Salt is present in Figure 1a, but its values are less than 0.01 μg m^{-3}.

generated from a distribution between ±2 g kg^{-1}. These perturbations are similar to those employed by *Donner et al.* [1999] and are chosen to be random so as not to impose organized structure on the convection when it develops.

3. Simulations

3.1. Aerosol

[26] The aerosol profiles for these simulations were extracted from a version of the GFDL AM2 [2004] nudged by NCEP re-analysis with aerosol chemistry. The details of the procedure for nudging the NCEP re-analysis are similar to *Timmreck and Schulz* [2004]. Aerosol chemistry is adopted from *Chin et al.* [2002] and *Koch and Rind* [1998]. Chemical reactions include DMS oxidation by OH during the day and by NO_3 during the night to form SO_2, and SO_2 oxidation by OH in the gas phase and by H_2O_2 in the aqueous phase to form sulfate. The predicted mass profiles, averaged over a 1-d period, are obtained at (36.61°N, 97.49°W) on 26 June 1997. Vertical profiles of the obtained aerosol, shown in Figure 1a, are used for the high-aerosol run. The low-aerosol run is conducted with aerosol profiles obtained by reducing these aerosol masses by a factor of 10. Sulfate, organic and salt aerosols are assumed to act only as CCN and to have trimodal lognormal size distributions. The mode diameter and standard deviation of the distributions, as well as the partitioning among modes, are assumed to follow the values of *Whitby* [1978] for clean continental air mass and not to vary spatiotemporally. Dust and BC aerosols are assumed to act only as IN with unimodal lognormal size distributions. For BC and dust, mode diameter and standard deviation are from the values of *Seinfeld and Pandis* [1998] for remote continental areas. As assumed for aerosols acting as CCN, mode diameter and standard deviation are assumed not to vary for those acting as IN. Aerosol number concentration in each bin of the size spectrum is determined based on aerosol mass and aerosol particle density for each species using the assumed lognormal size distribution at each grid point. Figure 1b shows the vertical profile of the sum of aerosol number concentration over all aerosol species and the CCN number concentration at a supersaturation of 1%. Total aerosol number concentration at the surface is ~4000 cm^{-3}, a typical value in clean continental areas [*Whitby*, 1978], and ~50% of aerosols are activated at a supersaturation of 1%. Depending on predicted aerosol mass within cloud, the total aerosol number for each aerosol species varies and is reset to the background value at all levels outside cloud. Within clouds, aerosols are advected, diffused, and depleted by nucleation. Initially aerosol mass mixing ratio is everywhere set equal to its background value. Background aerosol number concentrations for all aerosol species in each aerosol size mode are assumed not to vary during time integration, since the variation of the extracted aerosols from GFDL AM2 is not significant on the date of simulations.

3.2. Shear and Stability

[27] The different CAPE and shear simulations are generated by modifying the observed large-scale advection of temperature and specific humidity and the initial water vapor and wind fields. Identical humidity and temperature profiles from the ARM subcase A are applied as initial conditions, except for humidity at the lowest level, 0.5 km above the surface, in all environmental conditions (Figure 2). Since CAPE shows strong sensitivity to lowest-level humidity predominantly controlled by surface fluxes, initial humidity fields and humidity forcing at the lowest level are imposed differently to generate intended CAPE for each environmental condition. Humidity forcing above the lowest level is identical for all environmental conditions. Temperature forcing is identical at all levels in all environmental conditions except for the condition with CAPE less than 500 J kg^{-1}. The initial wind above 6 km in height is set equal to wind at 6 km, following *Wilhelmson and Klemp* [1978] who showed that low-level shear was more important to the development of modeled convection than upper-level shear. During the time integration, no large-scale forcing of wind is applied. Advective tendencies of potential temperature and humidity are imposed to generate the five different environmental conditions as follows.

[28] 1. High CAPE and strong wind shear: The initial average wind shear is set to 25 m s^{-1} over the lowest 6 km,

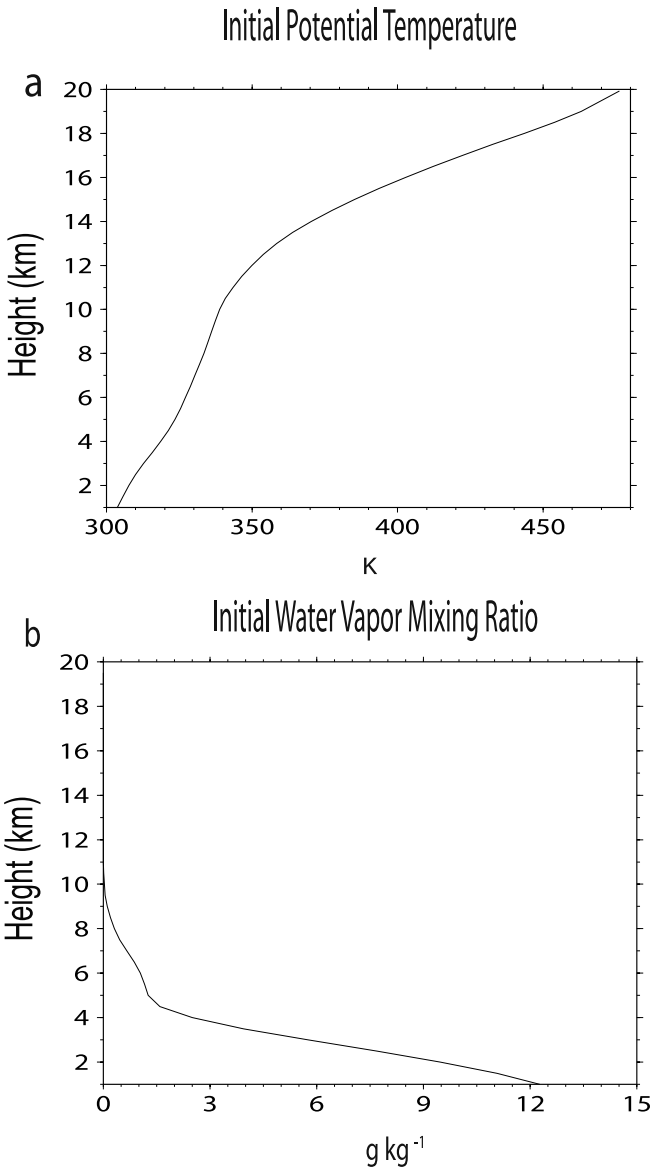

Figure 2. Vertical profiles of the initial conditions above the lowest level: (a) potential temperature and (b) water vapor mixing ratio.

and the advective tendencies generate a maximum CAPE of around 3000 J kg^{-1}. The wind shear is defined as the difference between density-weighted mean wind speed over the lowest 6 km of the profile and average wind speed over the lowest 500 m of the profile, following the definition of *Weisman and Klemp* [1982]. The vertical variation of initial horizontal wind is shown in Figure 3. Horizontal wind is 0 m s^{-1} at the lowest level and reaches 45 m s^{-1} at 6 km, equivalent to a mean vertical variation of 0.0075 m s^{-1} per meter. The potential temperature and humidity advective tendencies are depicted in Figures 4a, 4b, 4e, 4f, and 4g. Henceforth, this case is referred to as "High CAPE/Strong Shear."

[29] 2. High CAPE and weak wind shear: The potential temperature and humidity forcing is the same as for High CAPE/Strong Shear. However, the initial average wind shear is set to 10 m s^{-1} to isolate the role of wind shear by comparing with High CAPE/Strong Shear. The vertical variation of initial horizontal wind is shown in Figure 3. Horizontal wind is 0 m s^{-1} at the lowest level and reaches 20 m s^{-1} at 6 km, equivalent to a mean vertical variation of 0.0033 m s^{-1} per meter. Henceforth, this case is referred to as "High CAPE/Weak Shear."

[30] 3. Moderate CAPE and weak wind shear: The initial vertical variation of horizontal wind is the same as in High CAPE/Weak Shear, and the potential temperature forcing is the same as for High CAPE/Strong Shear and High CAPE/Weak Shear. To produce moderate CAPE of around 1500 J kg^{-1}, a humidity forcing of -12 g kg^{-1} d^{-1} is applied at the lowest level up to 16:40 UTC on 29 June, replacing the humidity forcing at the lowest level for High CAPE/Strong Shear and High CAPE/Weak Shear (depicted in Figure 4g). After this time, the humidity forcing at the lowest level of the atmosphere for High CAPE/Strong Shear, multiplied by a factor of 0.01, is applied. The lowest-level humidity forcing for this case is shown in Figure 4h. At the other levels, the same humidity forcing as for High CAPE/Strong Shear is applied. Henceforth, this case is referred to as "Moderate CAPE."

[31] 4. Low CAPE and weak wind shear: The initial wind shear is set to 1 m s^{-1}, and the maximum CAPE is around 500 J kg^{-1}, the lowest CAPE in the classification of *Bluestein* [1993]. The vertical initial wind variation is shown in Figure 3. The wind reaches 2.5 m s^{-1} at 6 km from 0 m s^{-1} at the lowest level, equivalent to a mean vertical variation of 0.0004 m s^{-1} per m. CAPE is generated with forcing of -51 g kg^{-1} d^{-1} up to 16:40 UTC on 29 June at the lowest level (Figure 4h). The same humidity forcing as for Moderate CAPE is applied at the lowest level after 16:40 UTC. The same humidity forcing as for High CAPE/Strong Shear is applied at the other levels. The same

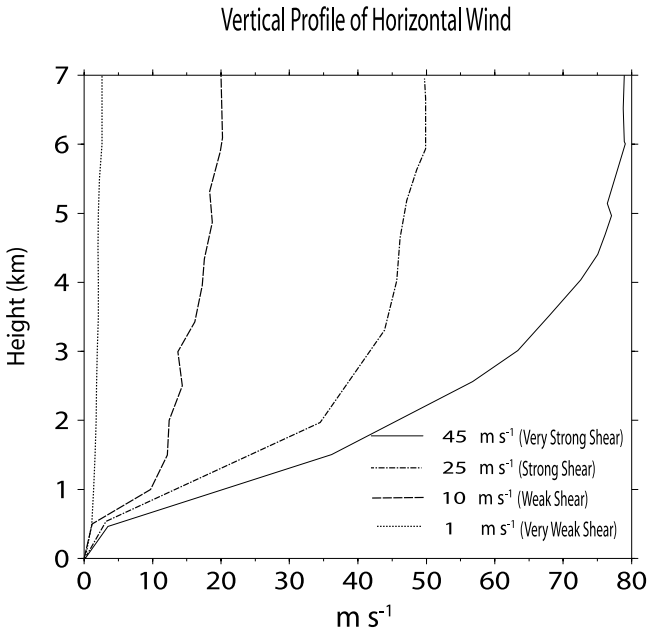

Figure 3. Vertical profiles of initial horizontal wind speed.

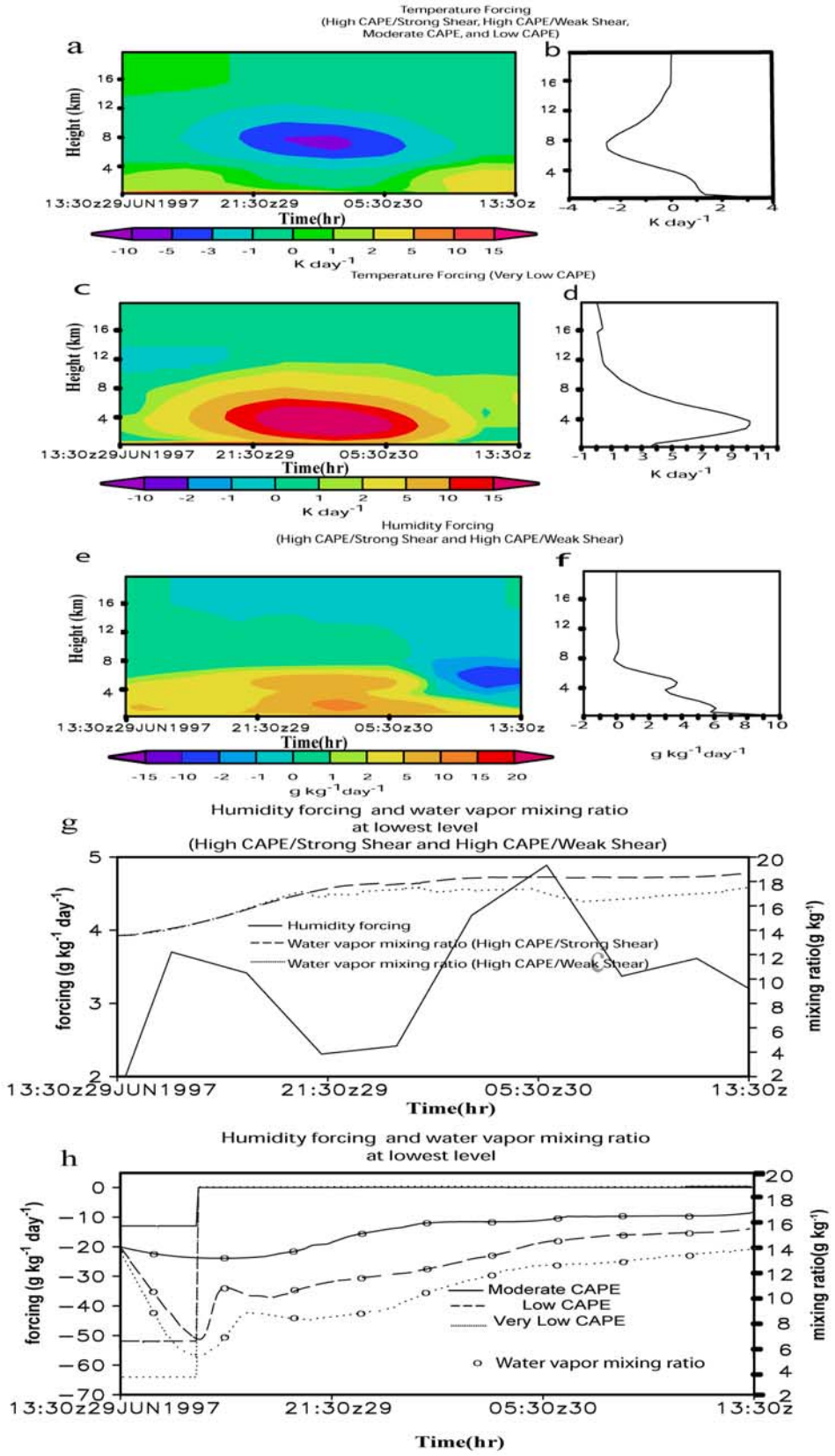
Temperature Forcing
(High CAPE/Strong Shear, High CAPE/Weak Shear,
Moderate CAPE, and Low CAPE)
a
b
Height (km)
Time(hr)
13:30z29JUN1997
21:30z29
05:30z30
13:30z
K day-1
Temperature Forcing (Very Low CAPE)
c
d
Humidity Forcing
(High CAPE/Strong Shear and High CAPE/Weak Shear)
e
f
g kg-1day-1
Humidity forcing and water vapor mixing ratio
at lowest level
(High CAPE/Strong Shear and High CAPE/Weak Shear)
g
forcing (g kg-1 day-1)
mixing ratio(g kg-1)
Humidity forcing
Water vapor mixing ratio (High CAPE/Strong Shear)
Water vapor mixing ratio (High CAPE/Weak Shear)
h
Moderate CAPE
Low CAPE
Very Low CAPE
Water vapor mixing ratio

Figure 4

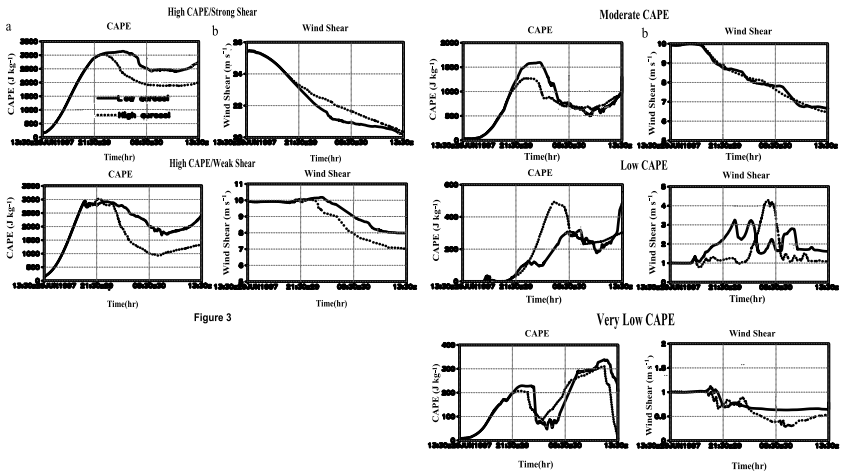

Figure 5. Time series of domain-averaged (a) CAPE (J kg^{-1}) and (b) wind shear (m s^{-1}).

potential temperature forcing as for High CAPE/Strong Shear is applied. Henceforth, this case is referred to as "Low CAPE."

[32] 5. Very low CAPE and weak wind shear: This condition is to simulate clouds with limited vertical extent. The maximum CAPE is set to 300 J kg^{-1} by applying the humidity forcing of -64 g kg^{-1} d^{-1} up to 16:40 UTC on 29 June at the lowest level (Figure 4h) and the potential temperature forcing shown in Figures 4c and 4d. The same initial wind vertical variation as in Low CAPE is adopted. After 16:40 UTC, the same humidity forcing at the lowest level as for Moderate CAPE and Low CAPE is applied. The humidity forcing is equal to that for the above four cases at the other levels. Henceforth, this is referred to as "Very Low CAPE."

[33] The negative forcing at the lowest level in the Moderate CAPE, Low CAPE, and Very Low CAPE lowers water vapor at the lowest level by offsetting the strong positive moisture flux at the surface prior to 16:40 UTC on 29 June. The vapor mixing ratio at the lowest level begins to rise around 16:40 UTC when the negative forcing is removed due to the surface moisture flux. Note that identical surface fluxes are prescribed in all conditions. Hence after the negative forcing is removed, the mixing ratio in the Moderate CAPE, Low CAPE, and Very Low CAPE stabilizes to a value lower than that in the High CAPE/Strong Shear and High CAPE/Weak Shear around 16:30 UTC (Figures 4g and 4h).

[34] The five sounding and advection sets for the corresponding environmental conditions, in conjunction with the dynamic, thermodynamic, and moisture tendencies produced by the simulated cloud system, determine the evolution of the temperature and moisture fields in WRF. Since the temperature and moisture evolve differently in each experiment, the CAPE and wind shear will also evolve differently, as shown in Figure 5. The different CAPEs and wind shears result in different cloud organizations leading to different reactions of the clouds to aerosols. Detailed discussion follows in section 4.1.

4. Results

[35] The ability of the model to simulate convective systems given observed forcing is demonstrated in Appendix B. Figure B1 shows modeled and observed precipitation for the ARM subcase A. Results from the five environmental conditions follow in the next sections.

4.1. CAPE, Wind Shear, Precipitation, and Cloud Organization

[36] Figure 6 shows the time series of the areal-mean cumulative rain and precipitation rate, and Figure 7, contours of mixing ratios of cloud liquid and cloud ice obtained around the occurrence of maximum precipitation rate in the high-aerosol run. These contours show cloud types at mature stages of cloud development. Figures 8a and 8b depicts the vertical profile of time- and domain-averaged cloud liquid and cloud ice in the high-aerosol run.

[37] Figure 5 shows the maximum CAPE of both the high- and low-aerosol runs in High CAPE/Strong Shear reaches around 3000 J kg^{-1}. The wind shear does not change much but shows a gradual decrease from 25 to around 20 m s^{-1} with no significant difference between the high- and low-aerosol runs throughout the time integration.

Figure 4. (a) Time-height cross section and (b) time- and domain-averaged vertical distribution of potential temperature large-scale forcing (K d^{-1}) for High CAPE/Strong Shear, High CAPE/Weak Shear, Moderate CAPE and Low CAPE. Figures 4c and 4d are the same as Figures 4a and 4b, respectively, but for Very Low CAPE. Figures 4e and 4f are time-height cross section and time- and domain-averaged vertical distribution of humidity large-scale forcing (g kg^{-1} $^{d-1}$), respectively, for High CAPE/Strong Shear and High CAPE/Weak Shear. Time series of humidity large-scale forcing and area-averaged water vapor mixing ratio at the lowest level of the atmosphere (g) for High CAPE/Strong Shear and High CAPE/Weak Shear and (h) for Moderate CAPE, Low CAPE and Very Low CAPE. For Figure 4h, circles indicate mixing ratio, while lines without circles indicate humidity forcing.

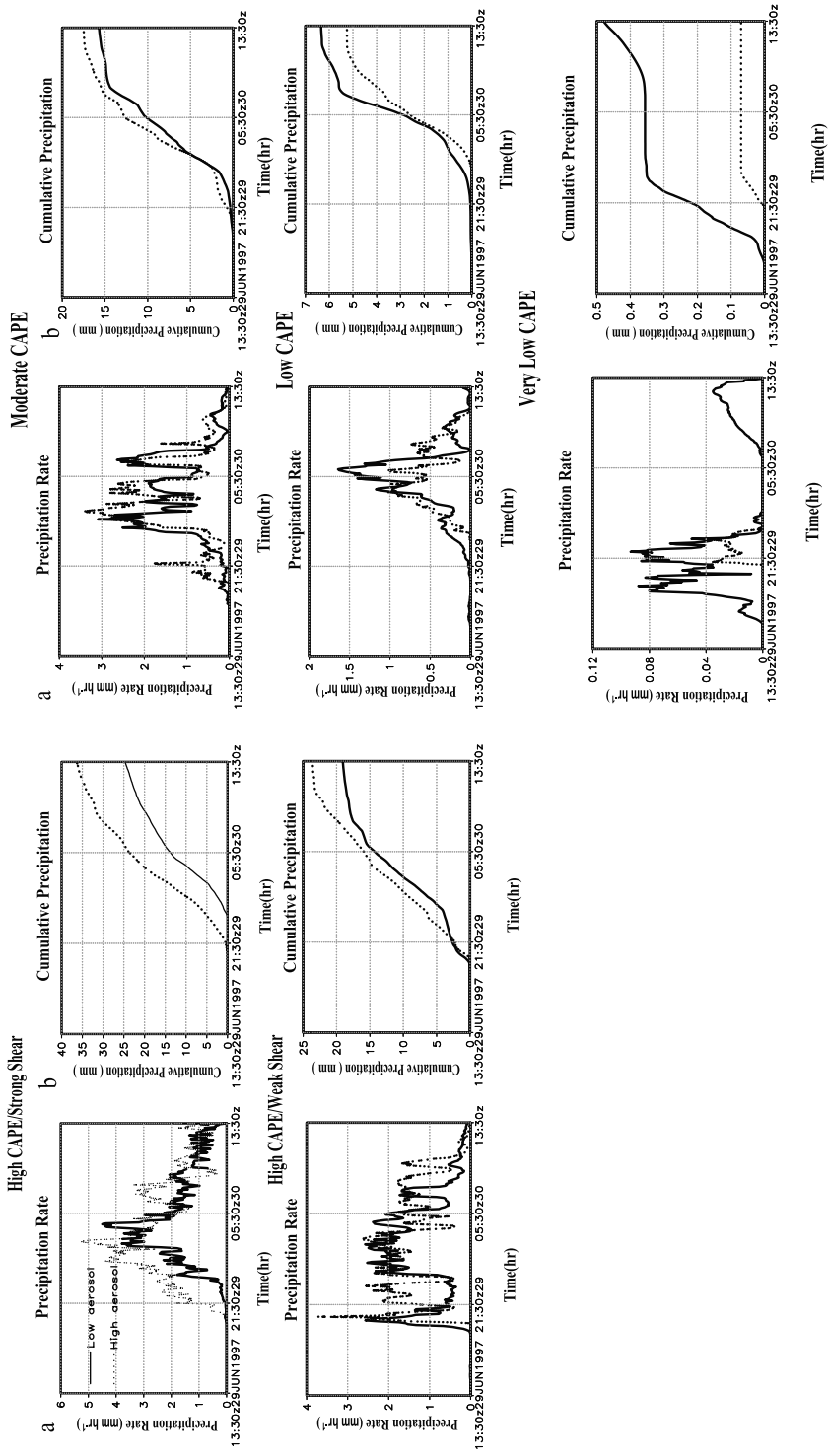

Figure 6. Time series of domain-averaged (a) precipitation rate (mm d^{-1}) and (b) cumulative rain (mm).

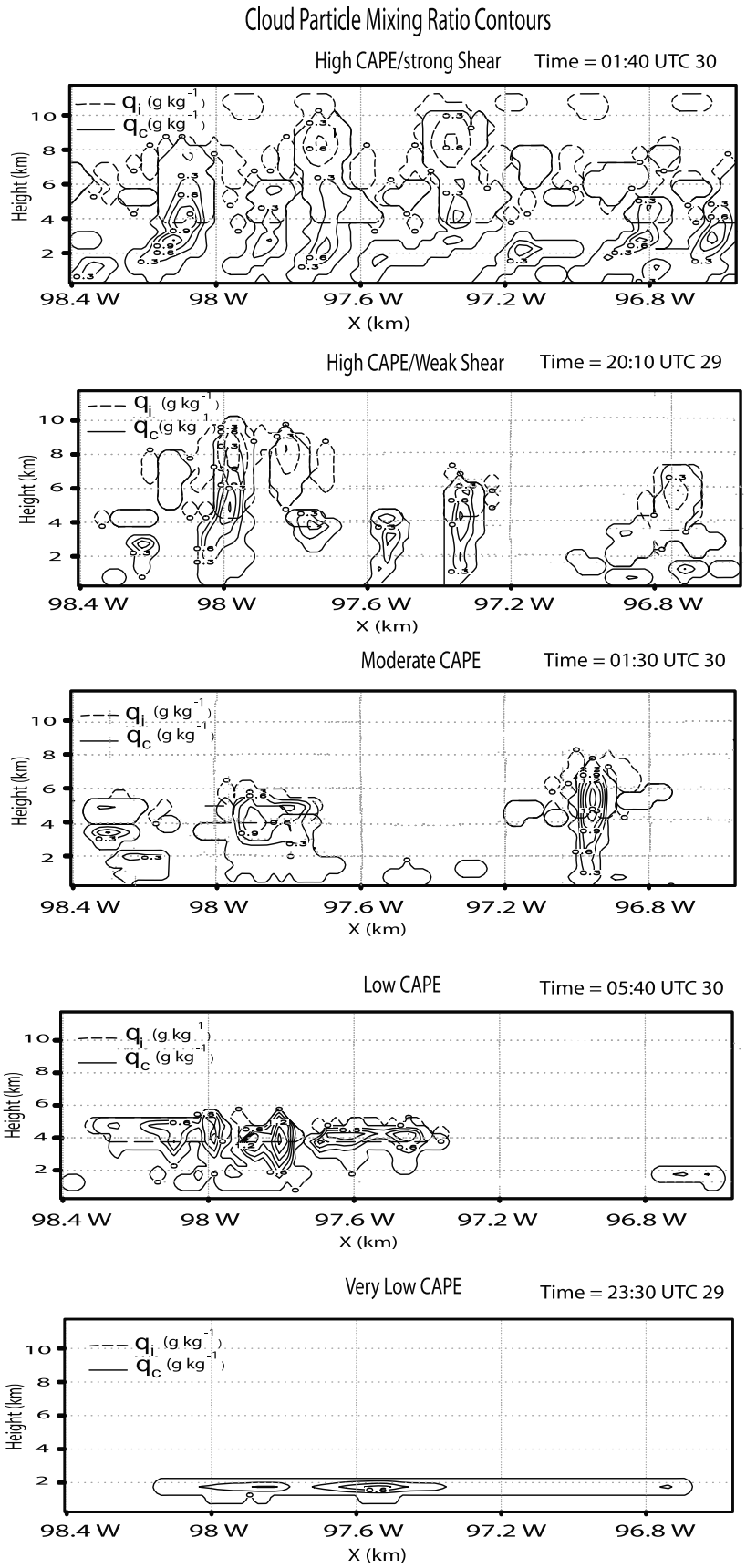

Figure 7. Contours of cloud liquid (solid line) and cloud ice (dashed line) (g kg^{-1}) at the time of the occurrence of maximum precipitation rate at high aerosol. Contour starts at 0 g kg^{-1} and contour interval is 0.3 g kg^{-1}.

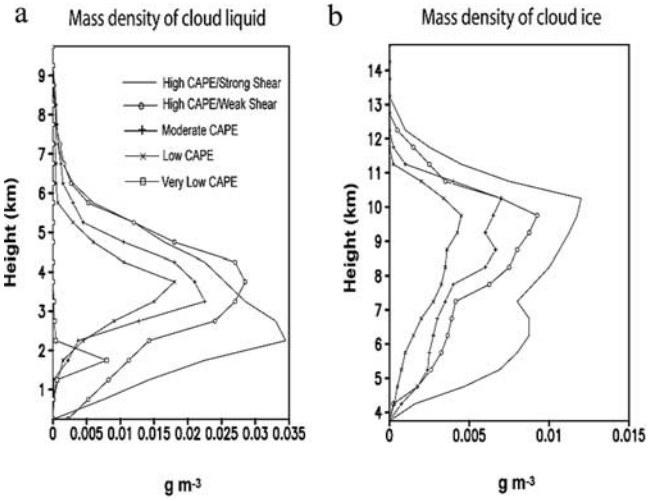

Figure 8. Vertical distribution of time- and domain-averaged mass concentration of (a) cloud liquid and (b) cloud ice in the high-aerosol run.

Under this condition, cumulonimbus- and cumulus-type clouds form (Figure 7) and cloud liquid and cloud ice show the largest values of the five environmental specifications (Figures 8a and 8b). Clouds start to form ~19:30 UTC on 29 June in both high- and low-aerosol runs. Accumulated precipitation is 24.49 mm in the low-aerosol run and 36.56 mm in the high- aerosol run, showing 49.28% more precipitation in the high-aerosol run.

[38] For High CAPE/Weak Shear, the maximum CAPE is around 3000 J kg^{-1}. Wind shear is between 7 and 10 m s^{-1} (Figure 5). Cumulonimbus- and cumulus-type clouds form with less frequency and intensity than in High CAPE/Strong Shear, as indicated in Figure 7. Clouds start to form ~19:00 UTC on 29 June in both high- and low-aerosol runs. Figures 8a and 8b show less cloud liquid and cloud ice in High CAPE/Weak Shear, as compared to those in High CAPE/Strong Shear, and cloud ice exists up to around 13 km (lower than in High CAPE/Strong Shear) due to weaker convection. The high-aerosol run shows more precipitation (23.57 mm) than the low-aerosol run (19.06 mm), but the difference is only 23.66%.

[39] For Moderate CAPE, the maximum CAPE in the low-aerosol run is around 1600 J kg^{-1}, about 250 J kg^{-1} larger than that in the high-aerosol run. As for High CAPE/Strong Shear and High CAPE/Weak Shear, the domain-averaged wind shear does not change much, gradually decreasing from 10 to 7 m s^{-1} (Figure 5). Cumulonimbus- and cumulus-type clouds form with less frequency and intensity than in the High CAPE/Strong Shear and High CAPE/Weak Shear, as indicated in Figures 7 and 8. Clouds start to form ~17:30 UTC on 29 June in both high- and low-aerosol runs. The high-aerosol run still shows more precipitation (17.52 mm) than the low-aerosol run (15.69 mm), but the difference is just 11.66%.

[40] The maximum CAPE for Low CAPE is around 500 J kg^{-1} in the both high- and low- aerosol runs. Low-level cumulus is the prevailing cloud type in Low CAPE (Figure 7). Clouds start to form ~17:00 UTC on 29 June in both high- and low-aerosol runs. The interesting point is that the accumulated precipitation in the high-aerosol run is less than that in the low-aerosol run, unlike that in the previous three pairs of experiments. The high-aerosol run shows 20.7% less precipitation (5.25 mm), compared to that in the low-aerosol run (6.34 mm).

[41] The percentage difference in the accumulated precipitation between the high- and low-aerosol runs is the largest for Very Low CAPE, where the maximum CAPE is around 300 J kg^{-1} in both the high- and low-aerosol runs. The dominant cloud types are low-level stratus with no cold microphysics, as indicated in Figures 7 and 8. Clouds start to form ~16:30 UTC on 29 June in both high- and low-aerosol runs. Cloud liquid is mostly around 2 km, and no cloud ice forms. The high-aerosol run shows 585.71% less precipitation (0.07 mm) than the low-aerosol run (0.48 mm).

[42] Precipitation starts later in high-aerosol run than in low-aerosol run in each environmental condition. This is due to higher CDNC (Table 2) at high aerosol, leading to delayed autoconversion. In High CAPE/Strong Shear, the initial precipitation rates are very small (less than 0.1 mm h^{-1}) at both aerosol concentrations, but the high-aerosol run quickly exhibits significantly heavier precipitation and continues to do so for nearly 8 h. We will return to this relative delay in the onset of heavy precipitation at low aerosol in section 4.3.

[43] CDNCs in Table 2 are obtained by conditionally averaging CDNC over grid points where cloud-liquid mixing ratio is nonzero. As CAPE decreases, updraft mass fluxes (Figure 9), vertical velocity of updrafts, and supersaturation decrease, leading to smaller CDNC at lower CAPE.

[44] We see the increase in aerosol number concentration causes precipitation enhancement or suppression, depending on environmental conditions and cloud types. In High CAPE/Strong Shear, High CAPE/Weak Shear and Moderate CAPE, cumulonimbi and cumuli formed with more precipitation at high aerosol. Comparison of High CAPE/Strong Shear and High CAPE/Weak Shear shows that reduced wind shear results in less organized and intense clouds with a smaller difference in precipitation between the high- and low-aerosol runs. As CAPE and wind shear become lower and weaker, the height of clouds lowers, and low-level cumulus and stratus begin to prevail, with more precipitation at low aerosol.

[45] More precipitation in the high-aerosol run indicates there are physical and dynamical processes contributing to the production of rain to compensate for reduction of rain by

Table 2. In-cloud Average CDNC for High and Low Aerosol Runs

		High CAPE/Strong Shear	High CAPE/Weak Shear	Moderate CAPE	Low CAPE	Very Low CAPE
CDNC (cm^{-3})	High Aerosol	753	353	135	52	21
	Low Aerosol	225	141	65	23	10

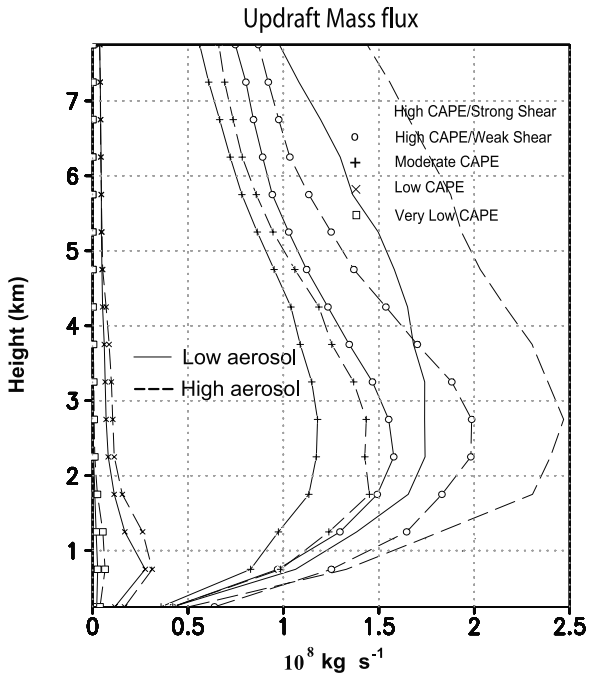

Figure 9. Vertical distribution of time-averaged updraft mass flux in convective regions.

retarded autoconversion. The high-aerosol runs show lower autoconversion in all environmental conditions due to higher CDNC (Table 2). The offsetting processes are not active enough to compensate for the reduced rain by autoconversion in Low CAPE and Very Low CAPE. Next, an analysis of the precipitation budgets is performed to identify the key microphysical processes leading to the different sensitivities of precipitation to aerosol number.

4.2. Precipitation Budget

[46] To elucidate microphysical processes leading to the differences in precipitation, differences in domain-averaged cumulative sources and sinks of precipitable hydrometeors between the high- and low-aerosol runs (high aerosol – low aerosol) are obtained. Production equations for precipitable hydrometeors are integrated over the domain and duration of the simulations (See the work of *Lin et al.* [1983] for production equations). The storage of the hydrometeors is zero (no suspended hydrometeors) at the end of the simulation, and, therefore, the time- and domain-average tendency is zero. The sources and sinks are shown in Table 3, referred to as the autoconversion-accretion form of the precipitation budget. In Table 3, the mixing ratios of water vapor, cloud liquid, cloud ice, rain, graupel, and snow are represented by q_v, q_c, q_i, q_r, q_g, and q_s, respectively, and *Au*, *A*, *Sh*, *De*, *E*, and *S* represent autoconversion, accretion, shedding, deposition, evaporation and sublimation, respectively. Pr is precipitation. Notation for terms in the table obeys the following conventions: The variable before the semicolon in each term indicates the quantity whose mixing ratio is changed by the source or sink. Following the semicolon, quantities that merge or separate in the source or sink are indicated by a "|" between them; a single variable following a semicolon indicates a quantity whose mixing ratio is changed by a phase transition. Volume and area integrations are denoted by $\langle\ \rangle$ and $||\ ||$, respectively:

$$\langle A\rangle = \frac{1}{Lx}\iiint \rho_a A dx dz dt,$$
$$\|A\| = \frac{1}{Lx}\iint A dx dt \tag{5}$$

Lx is the domain length (168 km).

[47] Table 3 shows increases and decreases in precipitation result from compensation among terms. Sources of negative (positive) difference and sinks of positive (negative) difference contribute to less (more) rain in the high-aerosol run. Among the sources and sinks, autoconversion and terms associated with accretion of cloud liquid predominantly account for precipitation differences. The sum of differences in those terms contributes to ~90% of precipitation differences in High CAPE/Strong Shear, High CAPE/Weak Shear, Moderate CAPE, and Low CAPE. Terms associated with accretion of cloud liquid are accretion of cloud liquid by rain, accretion of cloud liquid by graupel, accretion of cloud liquid by snow, shedding of cloud liquid from snow, shedding of cloud liquid from graupel, and accretion of cloud liquid by cloud ice. For Very Low CAPE, evaporation of rain is also an important process in the budget.

[48] In all cases in which higher aerosol leads to increased precipitation, the result stems from the increase in accretion (and shedding, for interactions between cloud liquid and snow or graupel) exceeding the decrease in autoconversion. The large increase in accretion requires the presence of increased cloud liquid. The source of the increased cloud liquid can be seen by replacing the terms in the budget in Table 3 (referred to as the autoconversion-accretion form of the precipitation budget) with the terms which balance them in the liquid water budget.

[49] The result is shown in Table 4, referred to as the condensation-evaporation form of the precipitation budget. In Table 4, *C*, *M*, *F*, and *HM* represent condensation, melting, freezing, and *Hallett and Mossop*'s [1974] rime-splintering. Table 4 shows differences in condensation and evaporation of cloud liquid are one to three orders of magnitude larger than the other terms. Therefore the difference in precipitation is approximated as follows for High CAPE/Strong Shear, High CAPE/Weak Shear, Moderate CAPE, Low CAPE, and Very Low CAPE:

$$\Delta\|\mathrm{Pr}\| \approx \Delta\langle C(q_c; q_v)\rangle - \Delta\langle E(q_v; q_c)\rangle \tag{6}$$

The terms on the right hand side of (6) are differences in condensation and evaporation, respectively. This formulation is also used by *Khain et al.* [2008]. The greater high-aerosol precipitation for High CAPE/Strong Shear, High CAPE/Weak Shear and Moderate CAPE is tied to greatly increased condensation of cloud liquid, which is greater than the increased evaporation of cloud liquid. In contrast, in Low CAPE and Very Low CAPE, increased condensation is smaller than increased evaporation of cloud liquid, leading to smaller precipitation in the high-aerosol run.

Table 3. Accumulated Sources and Sinks of Precipitation (Autoconversion-Accretion From), Averaged Over Domain

Sources and Sinks of Precipitation (mm): Autoconversion-Accretion Form					
	Differences (High Aerosol – Low Aerosol)				
	High CAPE/ Strong Shear	High CAPE/ Weak Shear	Moderate CAPE	Low CAPE	Very Low CAPE
	Sources				
$\langle Au(q_r; q_c \vert q_c)\rangle$ Autoconversion	−9.73	−8.41	−7.26	−3.79	−0.35
$\langle A(q_r; q_c \vert q_r)\rangle$ Accretion of cloud liquid By rain	9.29	5.41	3.29	1.50	−0.30
$\langle A(q_g; q_c \vert q_g)\rangle$ Accretion of cloud liquid by graupel	2.64	2.21	1.88	0.37	0.00
$\langle A(q_s; q_c \vert q_s)\rangle$ Accretion of cloud liquid By snow	6.77	3.73	2.59	0.50	0.00
$\langle Sh(q_r; q_c \vert q_s)\rangle + \langle Sh(q_r; q_c \vert q_g)\rangle$ Shedding of cloud liquid from snow or graupel	2.39	1.20	1.16	0.21	0.00
$\langle A(q_g; q_i \vert q_g)\rangle$ Accretion of cloud ice by graupel	0.13	0.05	−0.05	−0.08	0.00
$\langle Au(q_s; q_i \vert q_s)\rangle$ Accretion of cloud ice By snow	0.26	0.11	0.17	0.05	0.00
$\langle Au(q_s; q_i \vert q_i)\rangle$ Autoconversion of cloud ice	0.02	0.02	−0.08	−0.02	0.00
$\langle A(q_s; q_c \vert q_i)\rangle$ Accretion of cloud liquid by cloud ice	0.02	0.01	0.01	0.00	0.00
$\langle A(q_s; q_i \vert q_r)\rangle$ Accretion of cloud ice by rain to form snow	−0.06	0.03	−0.04	−0.05	0.00
$\langle A(q_g; q_i \vert q_r)\rangle$ Accretion of cloud ice by rain to form graupel	0.00	0.00	−0.01	−0.02	0.00
$\langle De(q_s; q_i)\rangle$ Depositional growth of cloud ice to form snow	0.07	0.05	0.02	−0.01	0.00
	Sinks				
$\langle E(q_v; q_r)\rangle$ Evaporation of rain	0.22	0.15	0.10	0.07	−0.24
$\langle S(q_v; q_s)\rangle$ Sublimation of snow	−0.45	−0.21	−0.13	−0.06	0.00
$\langle S(q_v; q_g)\rangle$ Sublimation of graupel	−0.04	−0.04	−0.12	−0.26	0.00
$\|\|Pr\|\|$ Precipitation	12.07	4.51	1.83	−1.09	−0.41

[50] Accretion of cloud liquid increases with increasing condensation. The sign of $\Delta||Pr||$ is determined by compensation among accretion of cloud liquid and autoconversion, except for Very Low CAPE where reduced evaporation of rain is the only compensation for reductions in both autoconversion and accretion. When the magnitude of the negative difference in autoconversion is smaller than that of the positive difference in the accretion, led by increasing condensation, precipitation is larger at high aerosol, as in High CAPE/Strong Shear, High CAPE/Weak Shear, and Moderate CAPE (see Table 3). In Low CAPE, increase in condensation and, thereby, in the accretion of cloud liquid are not large enough to compensate for the reduction in autoconversion, leading to more precipitation at low aerosol. Even the difference in the accretion of cloud liquid by rain is negative in Very Low CAPE (see Table 3).

[51] Cumulative precipitation normalized with respect to cumulative condensation is shown in Table 5. All high-aerosol runs show lower rates of rain production relative to condensation rates. The reduction in precipitation relative to condensation indicates the second indirect effect, i.e., aerosol suppression of precipitation through increasing CDNC. The increases in precipitation at high aerosol in High CAPE/Strong Shear, High CAPE/Weak Shear, and Moderate CAPE are made possible by an increase in condensation which dominates the reduced efficiency with which cloud liquid is converted to precipitation. In contrast, increases in condensation at high aerosol in Low CAPE and Very Low CAPE are insufficient, leading to decreases in precipitation. Increased condensation requires increased cooling, which can occur in updrafts associated with low-level convergence due to outflows from deep convective cells. The next section explores links between microphysics and dynamics in convective systems of different organization.

4.3. Dynamic Aspects

[52] As shown in the previous section, variations in condensation rate with increasing aerosol are important in determining whether increasing aerosol leads to precipitation enhancement or suppression. Table 4 shows the difference in the condensation between the high- and low-aerosol runs decreases as atmospheric stability increases. Figure 9 shows the time-averaged vertical profile of updraft mass flux in convective regions. The convective region includes a core and grid columns whose center is within 2 km of a core. A core satisfies at least one of the following three conditions: (1) maximum cloud draft strength (w_{max}) is larger than the average over grid columns within 4 km and w > 1 m s^{-1}, (2) w_{max} > 3 m s^{-1}, or (3) precipitation rate exceeds 25 mm h^{-1} [*Xu*, 1995].

[53] The difference in updrafts between the high- and low- aerosol runs decreases as CAPE and wind shear

Table 4. Accumulated Sources and Sinks of Precipitation (Condensation-Evaporation Form), Averaged Over Domain

Sources and Sinks of Precipitation (mm): Condensation-Evaporation Form					
	Difference (High Aerosol-Low Aerosol)				
	High CAPE/ Strong Shear	High CAPE/ Weak Shear	Moderate CAPE	Low CAPE	Very Low CAPE
	Sources				
$\langle C(q_c; q_v)\rangle$ Condensation	56.71	33.95	23.53	9.24	4.42
$\langle A(q_g; q_i \vert q_g)\rangle$ Accretion of cloud ice by graupel	0.13	0.05	−0.05	−0.08	0.00
$\langle A(q_s; q_i \vert q_s)\rangle$ Accretion of cloud ice By snow	0.26	0.11	0.17	0.05	0.00
$\langle M(q_c; q_i)\rangle$ Melting of cloud ice	0.01	0.04	0.01	0.02	0.00
$\langle Au(q_s; q_i \vert q_i)\rangle$ Autoconversion of cloud ice	0.02	0.02	−0.08	−0.02	0.00
$\langle A(q_s; q_i \vert q_r)\rangle$ Accretion of cloud ice by rain to form snow	−0.06	0.03	−0.04	−0.05	0.00
$\langle A(q_g; q_i \vert q_r)\rangle$ Accretion of cloud ice by rain to form graupel	0.00	0.00	−0.01	−0.02	0.00
$\langle De(q_s; q_i)\rangle$ Depositional growth of cloud ice to form snow	0.07	0.05	0.02	−0.01	0.00
	Sinks				
$\langle E(q_v; q_c)\rangle$ Evaporation of cloud liquid	46.58	30.39	22.05	10.60	5.15
$\langle F(q_i; q_c)\rangle$ Freezing of cloud liquid	−0.65	−0.40	−0.14	−0.10	0.00
$\langle HM(q_i; q_c \vert q_s)\rangle + \langle HM(q_i; q_c \vert q_g)\rangle$ Rime-splintering	−0.59	−0.15	−0.04	−0.03	0.00
$\langle E(q_v; q_r)\rangle$ Evaporation of rain	0.22	0.15	0.10	0.07	−0.32
$\langle S(q_v; q_s)\rangle$ Sublimation of snow	−0.45	−0.21	−0.13	−0.06	0.00
$\langle S(q_v; q_g)\rangle$ Sublimation of graupel	−0.04	−0.04	−0.12	−0.26	0.00
$\|\|\Pr\|\|$ Precipitation	12.07	4.51	1.83	−1.09	−0.41

become smaller, leading to smaller differences in condensation between the high- and low-aerosol runs. As shown by *Lee et al.* [2008], *Khain et al.* [2005], and *Lynn et al.* [2005], stronger updrafts and greater condensation at high aerosol are closely linked to the convergence field. Figure 10 shows the time series of domain-averaged $\left|\frac{\partial u}{\partial x}\right|$, a measure of the intensity of the convergence field, where u is horizontal wind velocity. (Note that the domain average of the divergence itself is zero, as it must be, given the use of periodic boundary conditions. The domain average of the absolute value of the divergence measures the intensity of localized regions of convergence and divergence with the domain.) The intensity of $\left|\frac{\partial u}{\partial x}\right|$ in both runs decreases as CAPE and shear are reduced, and the high-aerosol runs decrease more, leading to smaller differences in updraft and, thereby, condensation between the high- and low-aerosol runs. Greater evaporation of cloud liquid in the high-aerosol run, due to delayed autoconversion providing more abundant cloud liquid as a source of evaporation, is the reason for more intense convergence as shown by *Lee et al.* [2008], *Khain et al.* [2005], and *Lynn et al.* [2005]. More evaporation induces stronger downdrafts, and outflows associated with the stronger downdrafts generate stronger convergent regions. The increase in evaporation is smaller than the increase in condensation, which can be ascribed to humidity increases, in agreement with *Khain et al.* [2008]. In High CAPE/Strong Shear, values of relative humidity are 20% to 30% larger in the high-aerosol case for the last third or so of the integration around 6 km. A consequence of larger relative humidity where convection detrains is less evaporation there. The relative humidity also takes on larger values in the middle and lower troposphere for most of the integration in the high-aerosol case. In High CAPE/Strong Shear, the interactions among evaporation of detrained condensate, downdrafts, convergence, and formation of secondary clouds are especially favored, as can be seen in Figure 10. The magnitude of the convergence at high aerosol rapidly becomes much larger than at low aerosol, and this is reflected in relative delay in the development of heavy precipitation at low aerosol. As shown in Figure 11 and Table 4, the difference in evaporation of cloud liquid between the high- and low-aerosol

Table 5. Normalized Cumulative Precipitation With Respect to Cumulative Condensation at the End of Time Integration

		High CAPE/Strong Shear	High CAPE/Weak Shear	Moderate CAPE	Low CAPE	Very Low CAPE
Normalized Precipitation	High aerosol	0.31	0.32	0.30	0.20	0.01
	Low aerosol	0.40	0.48	0.45	0.38	0.19

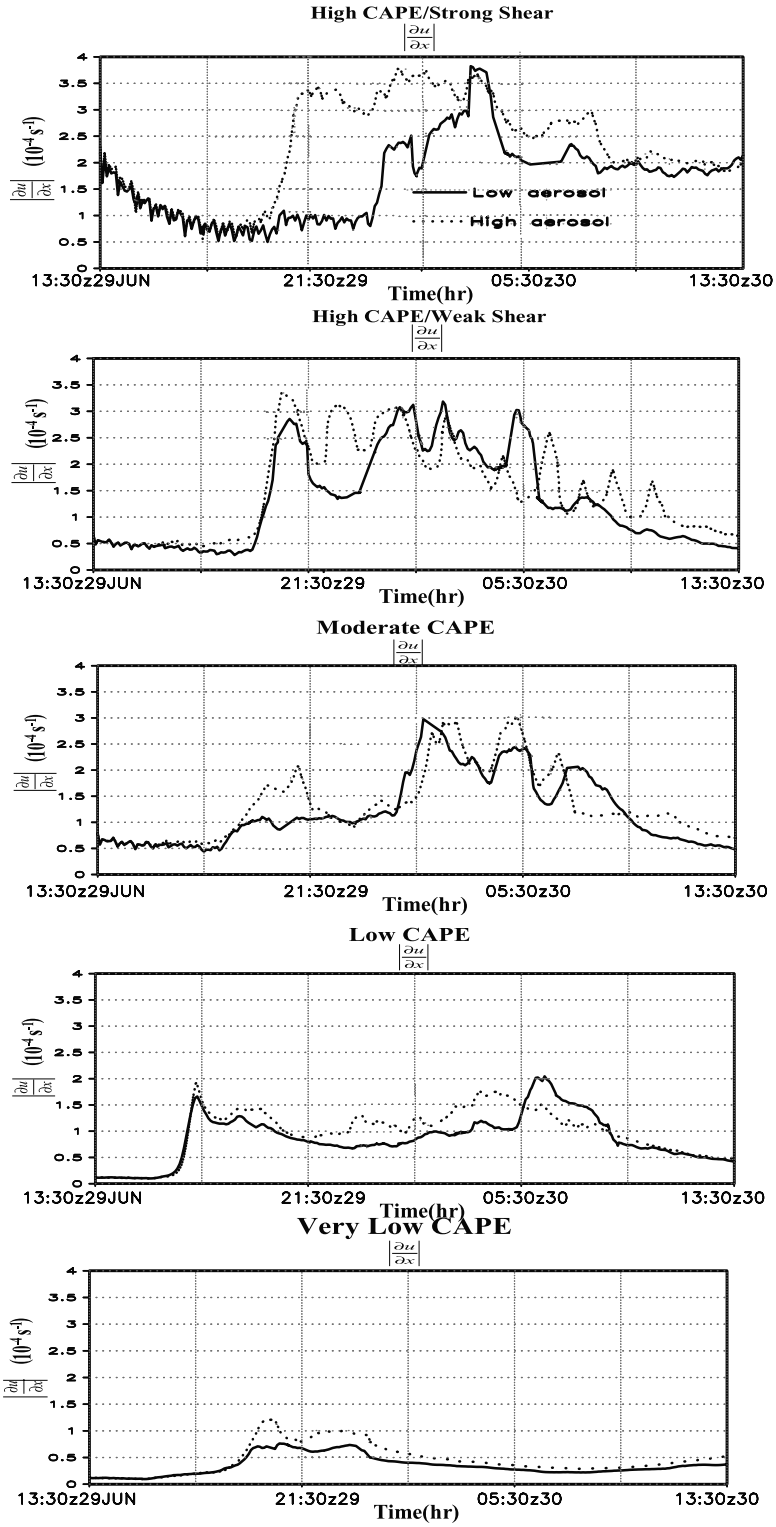

Figure 10. Time series of domain-averaged $\left|\frac{\partial u}{\partial x}\right|$, where u is horizontal wind velocity.

runs decreases sharply as CAPE decreases, leading to smaller difference in the intensity of convergence field and condensation. Reduced availability of cloud liquid, when the condensation difference between the high- and low-aerosol runs is small, limits accretion, and precipitation differences are then related to autoconversion differences.

4.4. Role of CDNC Variation in Evaporation

[54] The high-aerosol run is more affected by CAPE and shear than the low-aerosol run. The interactions between dynamics and microphysics weaken more at lower CAPE and shear in the high-aerosol run because evaporation is reduced more in the high-aerosol run. Reduced evaporation

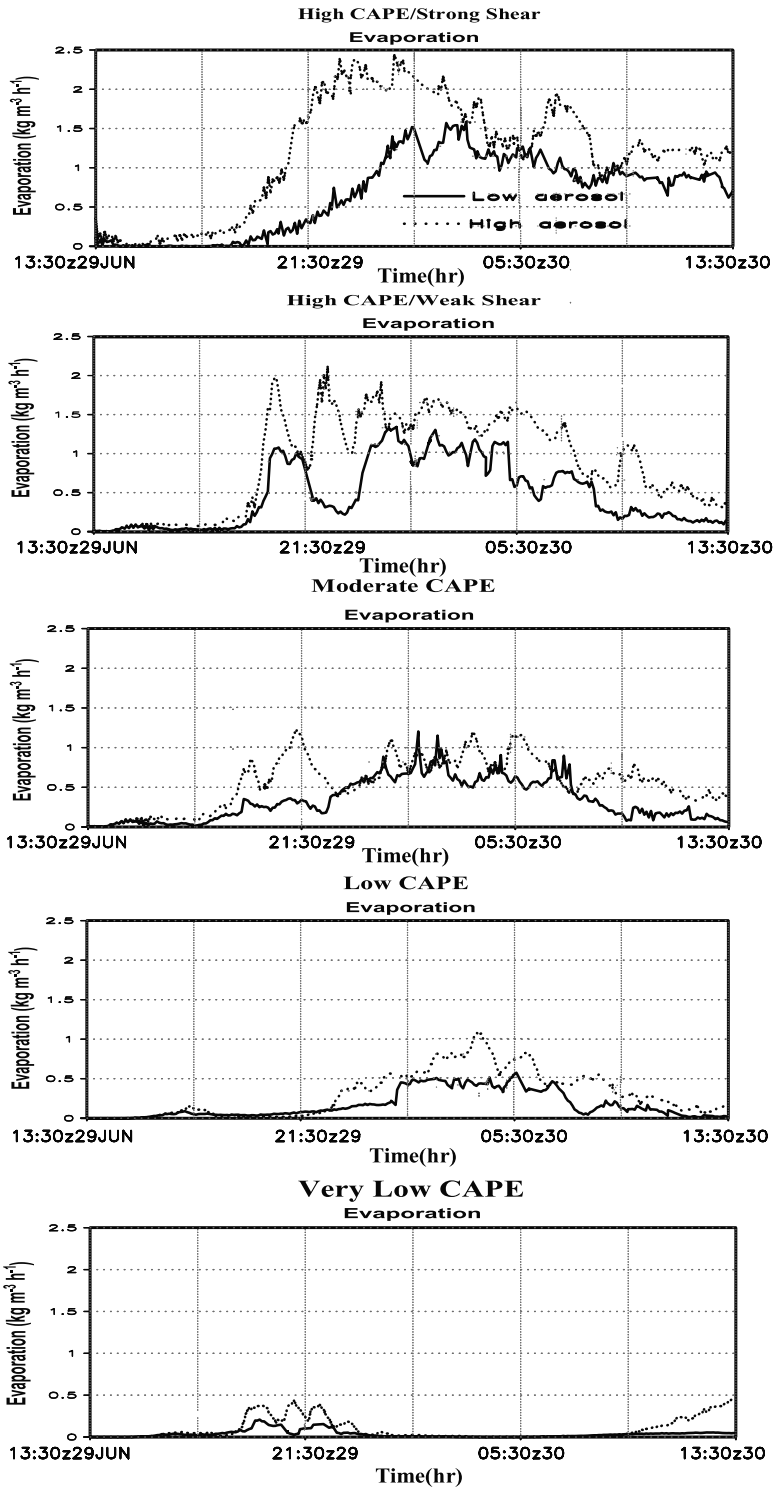

Figure 11. Time series of domain-averaged evaporation rate of cloud liquid.

reduces low-level convergence, updraft mass fluxes and condensation at high aerosol, with the difference in accretion of cloud liquid smaller or reversed. Reduced convective mass fluxes and environmental shear allow more cloud liquid to stay in saturated areas; the portion of cloud liquid transported to unsaturated areas decreases in the both high- and low-aerosol runs. This resulted in the decreased evaporation of cloud liquid. The decrease is greater at high aerosol due to larger decrease in transport of cloud liquid to unsaturated areas than at low aerosol with increasing stability.

[55] Larger reduction in CDNC and thereby autoconversion threshold with increasing stability at high aerosol (see Table 2) contributes to the larger reduction in evaporative

cooling at high aerosol. Increasing autoconversion of cloud liquid to rain due to the decreasing threshold reduces cloud liquid available for evaporation. To examine the role of larger reduction in CDNC at high aerosol in the difference in evaporative cooling and thereby low-level convergence between high- and low-aerosol runs, another set of simulations is performed. Identical CDNC difference is specified for the five environmental conditions. These simulations are compared to results of simulations with varying CDNC difference shown in previous sections. For the identical CDNC difference, mean CDNCs in High CAPE/Strong Shear (Table 2) are adopted. These CDNCs (753 cm^{-3} and 235 cm^{-3}) are applied to the autoconversion threshold as constants to ensure the identical spatiotemporal CDNC differences between the high- and low-aerosol runs for each environmental condition. Precipitation differences between high- and low-aerosol runs in High CAPE/Strong Shear, High CAPE/Weak Shear and Moderate CAPE are larger in this set of simulations than those shown in Figure 6. Precipitation differences are 66.32%, 33.67% and 22.89% in these experiments, respectively. This is because CDNC difference in this set of simulations is larger than mean CDNC differences in Table 2 for High CAPE/Weak Shear and Moderate CAPE, which leads to larger differences in evaporative cooling. Low-level convergence subsequently differs more between the high- and low-aerosol runs than shown in Figures 10 and 11. Note that High CAPE/Strong Shear still shows a larger precipitation difference than High CAPE/Weak Shear and Moderate CAPE,despite. Weaker detrainment and wind shear in High CAPE/Weak Shear and Moderate CAPE lead to less efficient transport of cloud liquid to unsaturated areas. This produces smaller differences in evaporative cooling as compared to that in High CAPE/Strong Shear. Also, the difference in downdrafts at the level of evaporative cooling is not magnified as much as in High CAPE/Strong Shear during descent to the surface, leading to smaller differences in low-level convergence, due to shallower cloud depth. Smaller cloud vertical extent and weaker wind shear and detrainment in High CAPE/Weak Shear and Moderate CAPE than in High CAPE/Strong Shear lead to smaller precipitation increase at high aerosol. This indicates the relative magnitude of increase in CDNC at high aerosol plays a secondary role in smaller precipitation increase at high aerosol in High CAPE/Weak Shear and Moderate CAPE than High CAPE/Strong Shear. Convective intensity and vertical extent are key factors for the different precipitation increases at high aerosol.

[56] In Low CAPE and Very Low CAPE with the identical CDNC difference, precipitation suppression is still observed with larger suppression in Very Low CAPE. High-aerosol runs show 12% and 825% less precipitation than low-aerosol runs in Low CAPE and Very Low CAPE, respectively. The CDNC and evaporation differences are larger than those in Table 2, but substantially weaker detrainment and smaller cloud vertical extent preclude a significant increase in low-level convergence. Smaller cloud vertical extent in Very Low CAPE leads to more substantial precipitation suppression than in Low CAPE. CDNC difference plays a secondary role in precipitation suppression at high aerosol in Low CAPE and Very Low CAPE (and their relative decreases), as compared to cloud vertical extent and detrainment.

4.5. Aerosol Effects at Very Strong Wind Shear

[57] This study shows proportionality between the intensity of convective clouds and wind shear (see Figure 9). However, *Weisman and Klemp* [1982] indicated that increasing wind shear could decrease the intensity of convection when the shear was extremely strong. This indicates that interactions between dynamics and microphysics and, thereby, effects of increasing aerosols on precipitation can be weakened at very strong wind shear. To examine aerosol effects on precipitation at very strong wind shear, a set of simulations was carried out with the same model setup as in High CAPE/Strong Shear but with an initial wind shear of 45 m s^{-1}, a maximum wind shear adopted by *Weisman and Klemp* [1982]. The vertical profile of initial horizontal wind for these experiments is shown in Figure 3. The wind speed reaches 79 m s^{-1} at 6 km from 0 m s^{-1} at the lowest level, equivalent to a mean vertical variation of 0.013 m s^{-1} per meter.

[58] The simulations show 31.35% larger precipitation at high aerosol. This increase in precipitation is smaller than that shown in High CAPE/Weak Shear. *Weisman and Klemp* [1982] indicated that high entrainment at very strong wind shear reduced the buoyancy of rising air parcels. This leads to reduced vertical extent of clouds, resulting in weakened interactions between dynamics and microphysics and a smaller increase in precipitation at high aerosol than that in High CAPE/Strong Shear.

4.6. Effects of Cold Microphysics

[59] As shown in Table 3, collection of cloud liquid by graupel played an important role in enhancing high-aerosol precipitation in High CAPE/Strong Shear, High CAPE/Weak Shear and Moderate CAPE. The sum of accretion of cloud liquid by snow and graupel is the largest percent of accretion of cloud liquid by precipitable hydrometeors in Moderate CAPE. To examine the role of cold microphysics, we have removed all ice processes in Moderate CAPE. The approximate difference equation (autoconversion-accretion form) of precipitation budget in the absence of cold microphysics is as follows:

$$\Delta\left\langle\frac{\partial q_r}{\partial t}\right\rangle = \Delta\|\mathrm{Pr}\| \approx \Delta\langle Au(q_r;q_c|q_c)\rangle + \Delta\langle A(q_r;q_c|q_r)\rangle$$
$$1.50 \qquad -7.30 \qquad 8.70 \qquad \mathrm{mm} \quad (7)$$

The contribution of evaporation of rain to precipitation difference is about one order of magnitude smaller than that of terms retained in (7). The other terms are associated with ice processes and, thus, do not contribute to precipitation difference. Autoconversion produces less rain at high aerosol, but accretion of cloud liquid by rain produces enough extra rain to overcome the deficit in autoconversion, which leads to more precipitation at high aerosol. The terms involving cloud liquid in (7) are replaced by the terms which balance them in the liquid-water budget to yield the approximate condensation – evaporation form of the precipitation budget:

$$\Delta\|\mathrm{Pr}\| \approx \Delta\langle C(q_c;q_v)\rangle - \Delta\langle E(q_v;q_c)\rangle$$
$$1.50 \qquad 30.15 \qquad 28.75 \qquad \mathrm{mm} \quad (8)$$

(8) indicates larger precipitation at high aerosol is associated with larger condensation as in the cases including cold microphysics. Normalized precipitation with respect to condensation at high aerosol (0.23) is lower than that at low aerosol (0.37) at the end of the integration, indicating more intense dynamics at high aerosol.

[60] As in the runs with cold microphysics, the high aerosol run shows more active near-surface convergence. This results from larger evaporation at high aerosol, leading to stronger downdraft mass fluxes and more intense convergence. The stronger convergence field causes more intense updraft activity and more condensation. The resultant increased cloud liquid generates more rain as it is collected by rain.

[61] The difference in precipitation is about 82% of that in the cases including cold microphysics. Cold microphysics increases the difference in precipitation, but it does not reverse the sign of the difference, indicating the more important role of interactions between dynamics and microphysics in enhancing precipitation at high aerosol.

5. Summary and Discussion

[62] To investigate the sensitivity of aerosol effects to shear and stability, pairs of numerical experiments were carried out. The experiments used an idealized framework, in which a two-dimensional cloud-system resolving model was integrated by imposing advective tendencies of potential temperature and vapor mixing ratio as time tendencies in the thermodynamic and moisture equations. These tendencies account for the thermodynamic and moisture effects of domain-mean convergence, while enabling the model to be integrated with periodic lateral boundary conditions. While this approach cannot simulate interactions between the modeled cloud system and larger-scale flows, it isolates interactions between aerosols, microphysics, and local dynamics (e.g., convergence fields within the model domain with zero domain-mean average). This approach enables the identification of microphysics-aerosol interactions on the scale of cloud systems. It remains for future study to represent these effects in larger-scale models, which will most likely require cumulus parameterizations with advanced microphysics, to understand the wider implications of the results obtained here.

[63] Use of a two-dimensional, rather than three-dimensional, cloud-system model affords substantial computational advantages but, as *Phillips and Donner* [2007] note, some aspects of the dynamics and microphysics differ in two- and three-dimensional models. *Phillips and Donner* [2007] found that vertical velocities and mass fluxes in deep convective updrafts, and downdraft mass fluxes, were larger in three dimensions than two dimensions. Downdrafts play an important role in the interactions between dynamics and microphysics described in this paper. The results of *Phillips and Donner* [2007] suggest this mechanism may have been underestimated in two dimensions. Conversely, *Phillips and Donner* [2007] also found that weak convective clouds were more numerous in two dimensions. To the extent these clouds play a role, they may be overestimated in two dimensions. A three-dimensional version of these experiments has also been conducted. Its CAPE and shear values are 2500 J kg^{-1} and 15 m s^{-1}, respectively, and single-moment microphysics, similar to *Phillips and Donner* [2007], was used. The high-aerosol run in this case behaved relative to the low-aerosol run similarly to the Moderate CAPE Experiment, with increased precipitation (13%), increased evaporation (150%), and increased domain-mean convergence magnitude (11%) in the high-aerosol run. Although the microphysics is highly simplified in the three-dimensional experiment, this result suggests that the qualitative character of the results does not depend on the dimensionality of the experiments.

[64] As does the choice of two dimensions, the choice of resolution (2 km horizontal, 500 m vertical) affords substantial computational advantages. *Donner et al.* [1999] reported a series of test calculations with a similar cloud-system model with resolutions ranging from 500 m to 5 km. They found basic features of the integrations (e.g., patterns of vertical velocity) were similar for horizontal resolutions of 2 km or finer. For shallower clouds, though, this resolution becomes more problematic.

[65] The model used in the paper does not have a scheme to keep track of aerosol size distribution within cumulus explicitly. The assumption of unchanged size distribution will lead to an overestimate of large CCN available for in-cloud nucleation. This type of nucleation is probably very weak in less vigorous convection with relatively low updrafts, so this assumption will not appreciably limit conclusions due to weaker convection. The assumption is more problematic for deep clouds but its impact applies to both the cases of high and low aerosol. The topic deserves further attention in future studies.

[66] This study does not take into account the removal of aerosols by precipitation (impaction scavenging). Impaction scavenging does not impact in-cloud nucleation strongly, but it can impact ice formation by reducing available IN. It is most effective when clouds develop heavy precipitation at their mature stages as shown by *Ekman et al.* [2004, 2006]. The key mechanisms leading to heavier precipitation with increasing aerosols begin to operate before heavy precipitation develops (see, Figures 6 and 10, which show the domain-mean convergence magnitude increases before the onset of heavy precipitation). Thus the neglect of impaction scavenging is not expected to change the qualitative nature of the results.

[67] For the simulation of shallow convective clouds such as warm cumulus and stratocumulus, high-resolution models such as Large Eddy Simulation (LES) have been used [*Stevens and Bretherton*, 2006; *Stevens et al.*, 2005; *Chlond and Wolkau*, 2000]. These models enable detailed simulation of entrainment and detrainment processes at cloud top, which play important roles in the evolution of shallow clouds and cannot be well- represented with a model whose resolution is as coarse as that employed here. Therefore the quantitative details of the precipitation changes associated with changes in aerosol concentration in the cases with shallow cumulus and stratus are of limited reality. Conceding this, these experiments still demonstrate that interactions between microphysics and dynamics whose strength is controlled by cloud vertical extent can vary widely. These variations, which are related to stability characteristics in which clouds form, are large enough to change the

sign of the precipitation change with increasing aerosol concentration.

[68] As *Khain et al.* [2008] indicated and shown in (6), precipitation changes are a small difference between two large terms, condensation and evaporation. Hence small errors in the calculation of those two terms can lead to significant errors in the evaluation of precipitation. Since the bulk scheme in this study dose not consider explicit changes in size distributions of cloud particles during evaporation, evaporation and, thereby, precipitation may not be evaluated as accurately as in bin models. Even bin models may fall short. For example, sublimation depends on the sizes of ice particles, and bin models remain problematic in calculating collision rates between ice particles and ice and liquid and accounting for the effects of turbulence. Moreover, larger evaporation and stronger near-surface convergence for precipitation enhancement at high aerosol simulated in the cases of high CAPE and strong wind shear were also simulated by recent bin-model studies [*Lynn et al.*, 2005; *Khain et al.*, 2005]. Delayed autoconversion and resultant evaporation of cloud liquid were essential for larger precipitation at high aerosol. Droplet nucleation played a predominant role in determining CDNC in the bin-model studies. High and low aerosol numbers, leading to high and low nucleating rates, were a primary cause of high and low CDNCs in high- and low-aerosol runs using bin microphysics, respectively, leading to delayed autoconversion in high-aerosol runs. The nucleation and autoconversion parameterizations in the bulk scheme were able to simulate CDNC differences for delayed autoconversion (and, thereby, precipitation enhancement at high aerosol) similar to those simulated using bin microphysics.

[69] With high CAPE and strong wind shear, cumulonimbus- and cumulus-type clouds were dominant and characterized by intense interactions between dynamics and microphysics. The interaction was much stronger in the high-aerosol run because more cloud liquid was transported to unsaturated areas, leading to more evaporation. More numerous, stronger downdrafts induced by the evaporation reached the surface to cause more intense convergence and, subsequently, more updraft activity and condensation. Increasing condensation and thereby accretion led to more precipitation by offsetting precipitation loss due to decreasing autoconversion and increasing evaporation at high aerosol. Strong wind shear and detrainment enabled effective transport of cloud liquid to unsaturated areas. Large vertical extent of clouds enabled development of strong downdrafts and convergence at high CAPE and strong wind shear. Cold microphysics magnifies the precipitation increase at high aerosol, but cold microphysics in these simulations, at least, is not essential to the precipitation increase. Detrainment of cloud liquid and associated evaporation were less with lower CAPE and wind shear, where dynamically weaker clouds dominated. Also, evaporatively driven differences in downdrafts at their level of initial descent were not magnified in clouds with shallow depth as much as in deep convective clouds as they accelerated to the surface over shorter distances. These weaker downdrafts led to reduced differences in low-level convergence, interactions between dynamics and microphysics, and, subsequently, condensation and accretion. Change in condensation and accretion of cloud liquid by precipitable hydrometeors at high aerosol in Low CAPE and Very Low CAPE did not balance the decreased autoconversion and increased evaporation at high aerosol and resulted in less precipitation.

[70] There are studies showing precipitation suppression at high aerosol in deep convective clouds in Texas, CCOPE, and Amazon cases [*Khain and Pokrovsky*, 2004; *Khain et al.*, 2004, 2008; *Cui et al.*, 2006; *Phillips et al.*, 2007b]. These studies indicate the mechanisms which increase precipitation with increasing aerosol in the cases with high CAPE and wind shear in this study do not operate in all cases. *Khain et al.* [2008] identified humidity as another crucial factor. In cumulus clouds in those studies, the increase in condensation was less than that in evaporation as in Low CAPE, leading to precipitation suppression at high aerosol. However, for deep convective clouds simulated in High CAPE/Strong Shear and High CAPE/Weak Shear, evaporation of cloud liquid and development of downdrafts were more effective than those in cumulus clouds. Significantly increased condensation at high aerosol resulted, as shown in the ARM deep convective case by *Lee et al.* [2008] and squall line cases by *Khain et al.* [2005] and *Lynn et al.* [2005]. The extent of the precipitation-increasing interactions in these High-CAPE experiments can be limited by other atmospheric characteristics. Additional factors which can control the formation of precipitation-increasing secondary clouds include humidity, boundary layer properties, and cloud base heights. If formation of precipitation-increasing secondary clouds is sufficiently limited, the effect of increased evaporation and sublimation will be to reduce precipitation.

[71] Reduction in CDNC difference between high- and low-aerosol runs played a secondary role in the reduction in difference in evaporative cooling with increasing stability. Although constant CDNC differences between high- and low-aerosol runs were imposed in another set of simulations, evaporation-stability and precipitation-aerosol relationships similar to those with variable CDNC differences were obtained. This indicated variation of wind shear, detrainment and cloud vertical extent played more important roles than the variation of CDNC difference.

[72] At very strong wind shear, the effect of entrainment on the buoyancy of rising air parcels reduced the intensity of interactions between dynamics and microphysics, leading to smaller dependence of precipitation on aerosols than in High CAPE/Strong Shear. Wind shear variation from High CAPE/Strong Shear to Very Low CAPE covered the range of observed shear considered by *Marwitz* [1972], which adopted typical wind shear in real atmosphere.

[73] The idealized modeling here shows that variations in CAPE and wind shear can produce a range of convective responses to aerosols through the formation of secondary clouds. However, variations of this nature do not preclude other interactions or thermodynamic factors as controls on the response of convection to variations in aerosols. For example, *Khain et al.* [2008] found that increasing aerosol can either decrease or increase surface precipitation, depending on humidity. Also, a given value of CAPE is not unique with respect to thermodynamic structure. For example, CAPE can be increased by increasing near-surface

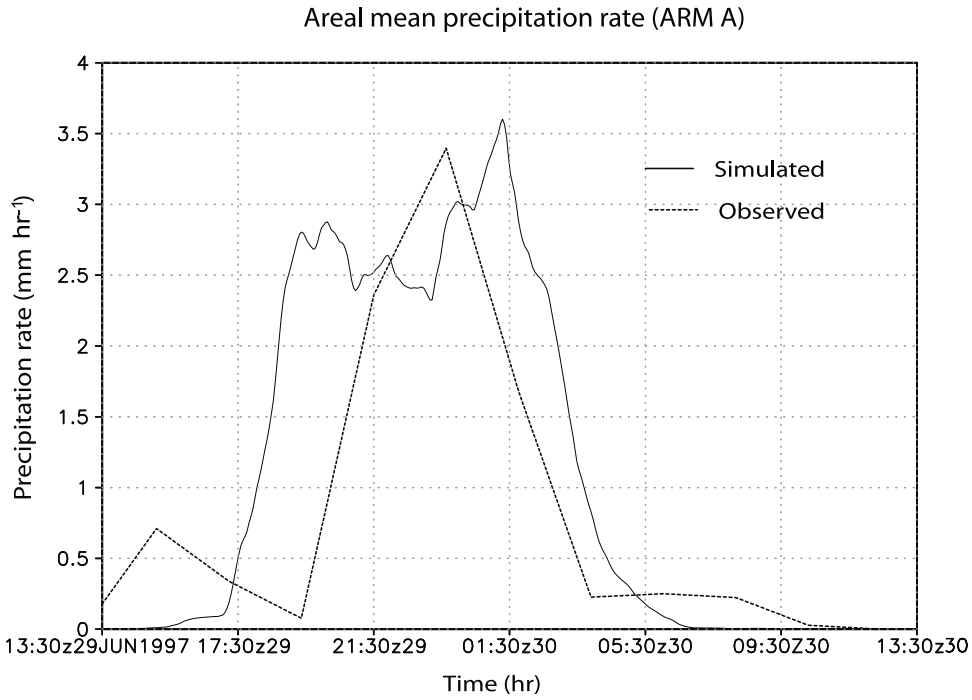

Figure B1. Time series of the areal-mean precipitation rate in ARM subcase A.

humidity or by increasing the middle-tropospheric lapse rate. The former approach has been used to generate the idealized CAPE increases in this paper. Increasing the CAPE in this way particularly favors increased condensate production with increasing aerosols and the subsequent interactions described here.

Appendix A: Deposition Nucleation at Temperatures Warmer Than −40°C

[74] At temperatures between −30 and −40°C and between −5 and −30°C, the parameterizations of *DeMott et al.* [2003] and *Meyers et al.* [1992], multiplied by a scaling factor, are used for deposition nucleation, respectively. For temperatures between −30 and −40°C:

$$N_{IN}\left(\mathrm{m}^{-3}\right) = 1000(\exp[12.96(S_i - 1.1)])^{0.3} \times \Psi \qquad \text{(A1)}$$

Here, N_{IN} is ice-crystal number concentration, S_i the saturation ratio with respect to ice and Ψ a scaling factor to take into account the dependence of IN activation on dust mass. Ψ is $\frac{DU_{2.5}}{DU^*_{2.5}}$, where $DU_{2.5}$ is mass concentration of dust particles with diameter less than 2.5 μm and $DU^*_{2.5}$ is a reference dust mass concentration. $DU^*_{2.5}$ is set at 0.11 μg m^{-3} based on dust data from the Mount Werner project used to derive (A1) [*DeMott et al.*, 2003]. Hence (A1) computes N_{IN} based on variation of dust mass relative to dust mass observed at the Mount Werner project. It was observed that IN concentrations were almost linear with the concentrations of large aerosol particles [*Berezinskiy et al.*, 1986; *Georgii and Kleinjung*, 1967], supporting the assumption that N_{IN} is proportional to $DU_{2.5}$. For temperatures between −5 and −30°C, the same scaling factor as used in (A1) is applied to the parameterization of *Meyers et al.* [1992] as follows, since dust mass data are not available in the work of *Meyers et al.* [1992]:

$$N_{IN}\left(\mathrm{m}^{-3}\right) = 63\exp[12.96(S_i - 1) - 0.639] \times \Psi \qquad \text{(A2)}$$

Appendix B: Simulation With Observed Forcing From ARM Subcase A

[75] To evaluate performance of CSRM adopted here, a simulation is conducted using the observed forcing from ARM subcase A. The same model setup as for the high-aerosol runs are applied to this simulation except that ARM subcase A observations provide initial fields and large-scale forcing.

[76] Figure B1 depicts the time series of the area-mean precipitation rate smoothed over 3 h for the entire domain for ARM subcase A. The model simulates precipitation reasonably well.

[77] **Acknowledgments.** The authors wish to thank Venkatachalam Ramaswamy for valuable discussions. Our thanks also go to Paul Ginoux and Charles Seman for providing us aerosol profiles and postprocessors, respectively. This paper was prepared under award NA17RJ2612 from the National Oceanic and Atmospheric Administration, U.S. Department of Commerce. The statements, findings, conclusions, and recommendations are those of the authors and do not necessarily reflect the views of the National Oceanic and Atmospheric Administration, or the U. S. Department of Commerce.

References

Abdul-Razzak, H., and S. J. Ghan (2000), A parameterization of aerosol activation: 2. Multiple aerosol types, *J. Geophys. Res.*, *105*, 6837–6844.

Albrecht, B. A. (1989), Aerosols, cloud microphysics, and fractional cloudiness, *Science*, *245*, 1227–1230.

Berezinskiy, N. A., G. V. Stepanov, and V. G. Khorguani (1986), Altitude variation of relative ice-forming activity of natural aerosol, *S. Meteorol. Hydrol.*, *12*, 86–89.

Bluestein, H. B. (1993), *Synoptic-Dynamic Meteorology in Midlatitudes: Volume II: Observations and Theory of Weather Systems (Synoptic-Dynamic Meteorology in Midlatitudes)*, 594 pp., Oxford Univ. Press, New York.

Chen, S.-H., and J. Dudhia (2000), *Anuual Report: WRF Physics*, 38 pp., Air Force Weather Agency, Boulder.

Chin, M., et al. (2002), Tropospheric aerosol optical thickness from the GOCART model and comparisons with satellite and Sun photometer measurements, *J. Atmos. Sci.*, *59*, 441–460.

Chlond, A., and A. Wolkau (2000), Large-eddy simulation of nocturnal stratocumulus topped marine atmospheric boundary layer: An uncertainty analysis, *Boundary Layer Meteorol.*, *95*, 31–35.

Cui, Z., K. S. Carslaw, Y. Yin, and S. Davies (2006), A numerical study of aerosol effects on the dynamics and microphysics of a deep convective clouds in a continental environment, *J. Geophys. Res.*, *111*, D05201, doi:10.1029/2005JD005981.

DeMott, P. J., D. J. Cziczo, A. J. Prenni, D. M. Murphy, S. M. Kreidenweis, D. S. Thomson, R. Borys, and D. C. Rogers (2003), Measurements of the concentration and composition of nuclei for cirrus formation, *Proc. Natl. Acad. Sci. U.S.A.*, *100*(25), 14,655–14,660.

Donner, L. J., C. J. Seman, and R. S. Hemler (1999), Three-dimensional cloud-system modeling of GATE convection, *J. Atmos. Sci.*, *56*, 1885–1912.

Ekman, A. M. L., C. Wang, J. Wilson, and J. Ström (2004), Explicit simulations of aerosol physics in a cloud-resolving model: A sensitivity study based on an observed convective cloud, *Atmos. Chem. Phys.*, *4*, 773–791.

Ekman, A. M. L., C. Wang, J. Wilson, J. Ström, and R. Krejci (2006), Explicit simulation of aerosol physics in a cloud-resolving model: Aerosol transport and processing in the free troposphere, *J. Atmos. Sci.*, *63*, 682–696.

Facchini, M. C., M. Mircea, S. Fuzzi, and R. J. Charlson (1999), Cloud albedo enhancement by surface-active organic solutes in growing droplets, *Nature*, *401*, 257–259.

Field, P. R., O. Möhler, P. Connolly, M. Krämer, R. Cotton, A. J. Heymsfield, H. Saathoff, and M. Schnaiter (2006), Some ice nucleation characteristics of Asian and Saharan desert dust, *Atmos. Chem. Phys.*, *6*, 2991–3006.

Freidenreich, S. M., and V. Ramaswamy (1999), A new multiple-band solar radiative parameterization for general circulation models, *J. Geophys. Res.*, *104*, 31,389–31,410.

Georgii, H. W., and E. Kleinjung (1967), Relations between the chemical composition of atmospheric aerosol particles and the concentration of natural ice nuclei, *Atmos. Res.*, *3*, 145–146.

Grabowski, W. W. (2006), Indirect Impact of atmospheric aerosols in idealized simulations of convective-radiative quasi equilibrium, *J. Clim.*, *18*, 4664–4682.

Gunn, R., and B. B. Phillips (1957), An experimental investigation of the effect of air pollution on the initiation of rain, *J. Atmos. Sci.*, *56*, 272–280.

Hallett, J., and S. C. Mossop (1974), Production of secondary ice particles during the riming process, *Nature*, *249*, 26–28.

Hong, S.-Y., and H.-L. Pan (1996), Nonlocal boundary layer vertical diffusion in a medium range forecast model, *Mon. Weather Rev.*, *124*, 2322–2339.

Hong, S.-Y., Y. Noh, and J. Dudhia (2006), A new vertical diffusion package with an explicit treatment of entrainment processes, *J. Atmos. Sci.*, *24*, 2318–2341.

Houze, R. A. (1993), *Cloud Dynamics*, 573 pp., Elsevier, New York.

Khain, A., and A. Pokrovsky (2004), Simulation of effects of atmospheric aerosols on deep turbulent convective clouds using a spectral microphysics mixed-phase cumulus cloud model. part II: Sensitivity study, *J. Atmos. Sci.*, *24*, 2983–3001.

Khain, A., A. Pokrovsky, M. Pinsky, A. Seifert, and V. Phillips (2004), Simulation of effects of atmospheric aerosols on deep turbulent convective clouds using a spectral microphysics mixed-phase cumulus cloud model. part I: Model description and possible applications, *J. Atmos. Sci.*, *15*, 2963–2982.

Khain, A., D. Rosenfeld, and A. Pokrovsky (2005), Aerosol impact on the dynamics and microphysics of deep convective clouds, *Q. J. R. Meteorol. Soc.*, *131*, 2639–2663.

Khain, A., N. BenMoshe, and A. Pokrovsky (2008), Factors determining the impact of aerosols on surface precipitation from clouds: Attempt of classification, *J. Atmos. Sci.*, *65*, 1721–1748.

Klemp, J. B., W. C. Skamarock, and J. Dudhia (2007), Conservative split-explicit time integration methods for the compressible nonhydrostatic equations, *Mon. Weather Rev.*, *135*, 2897–2913.

Koch, D., and D. Rind (1998), Beryllium 10/beryllium 7 as a tracer of stratospheric transport, *J. Geophys. Res.*, *103*(D4), 3907–3917.

Leaitch, W. R., J. W. Strapp, and G. A. Isaac (1986), Cloud droplet nucleation and cloud scavenging of aerosol sulfate in polluted atmosphere, *Tellus, Ser. A*, *38B*, 328–344.

Lee, S. S., L. J. Donner, V. T. J. Phillips, and Y. Ming (2008), Examination of aerosol effects on precipitation in deep convective clouds during the 1997 ARM summer experiment, *Quart. J. Roy. Meteor. Soc.*, in press.

Lin, Y. L., R. D. Farley, and H. D. Orville (1983), Bulk parameterization of the snow field in a cloud model, *J. Appl. Meteorol.*, *19*, 1065–1092.

Lohmann, U., and K. Diehl (2006), Sensitivity studies of the importance of dust ice nuclei for the indirect aerosol effect on stratiform mixed-phase clouds, *J. Atmos. Sci.*, *63*, 968–982.

Lohmann, U., J. Feichter, C. C. Chuang, and J. E. Penner (1999), Prediction of the number of cloud droplets in the ECHAM GCM, *J. Geophys. Res.*, *104*(D8), 9169–9198.

Lynn, B. H., A. P. Khain, J. Dudhia, D. Rosenfeld, A. Pokrovsky, and A. Seifert (2005), Spectral (bin) microphysics coupled with a mesoscale model (MM5). part I: Model description and first results, *Mon. Weather Rev.*, *133*, 44–58.

Marwitz, J. D. (1972), The structure and motion of severe hailstorms. part I: Supercell storms, *J. Appl. Meteorol.*, *11*, 166–179.

Meyers, M. P., P. J. DeMott, and W. R. Cotton (1992), New primary ice-nucleation parameterization in an explicit cloud model, *J. Appl. Meteorol.*, *31*, 708–720.

Michalakes, J., S. Chen, J. Dudhia, L. Hart, J. Klemp, J. Middlecoff, and W. Skamarock (2001), Development of a next generation regional weather research and forecast model, in *Developments in Teracomputing: Proceedings of the Ninth ECMWF Workshop on the Use of High Performance Computing in Meteorology*, edited by W. Zwieflhofer and N. Kreitz, pp. 269–276, World Sci., Singapore.

Ming, Y., V. Ramaswamy, L. J. Donner, and V. T. J. Phillips (2006), A new parameterization of cloud droplet activation applicable to general circulation models, *J. Atmos. Sci.*, *63*, 1348–1356.

Möhler, O., et al. (2006), Efficiency of the deposition mode ice nucleation on mineral dust particles, *Atmos. Chem. Phys.*, *6*, 3007–3021.

Morrison, H., and W. W. Grabowski (2007), Comparison of bulk and bin warm-rain microphysics models using a kinematic framework, *J. Atmos. Sci.*, *64*, 2839–2861.

Nenes, A., and J. H. Seinfeld (2003), Parameterization of cloud droplet formation in global climate model, *J. Geophys. Res.*, *108*(D14), 4415, doi:10.1029/2002JD002911.

Phillips, V. T. J., and L. J. Donner (2007), Cloud microphysics, radiation, and vertical velocities in two- and three-dimensional simulations of deep convection, *Q. J. R. Meteorol. Soc.*, *133*, 3011–3033.

Phillips, V. T. J., L. J. Donner, and S. Garner (2007a), Nucleation processes in deep convection simulated by a cloud-system-resolving model with double-moment bulk microphysics, *J. Atmos. Sci.*, *64*, 738–761.

Phillips, V. T. J., A. Pokrovsky, and A. Khain (2007b), The influence of time-dependent melting on the dynamics and precipitation production in maritime and continental storm clouds, *J. Atmos. Sci.*, *64*, 338–359.

Pruppacher, H. R., and J. D. Klett (1978), *Microphysics of Clouds and Precipitation*, 714 pp., Springer, New York.

Saleeby, S. M., and W. R. Cotton (2004), A large-droplet mode and prognostic number concentration of cloud droplets in the Colorado state university regional atmospheric modeling system (RAMS). part I: Module description and supercell test simulations, *J. Appl. Meteorol.*, *43*, 182–195.

Schwazkopf, M. D., and V. Ramaswamy (1999), Radiative effects of CH_4, N_2O, halocarbons and the foreign-broadened H_2O continuum: A GCM experiment, *J. Geophys. Res.*, *104*, 9467–9488.

Seinfeld, J. H., and S. N. Pandis (1998), *Atmospheric Chemistry and Physics: From Air Pollution to Climate Change*, 1326 pp., John Wiley, Hoboken, N. J.

Stevens, D. E., and C. S. Bretherton (2006), Effects of resolution on the simulation of stratocumulus entrainment, *Q. J. R. Meteorol. Soc.*, *125*, 425–439.

Stevens, B., et al. (2005), Evaluation of large-eddy simulations via observations of nocturnal marine stratocumulus, *Mon. Weather Rev.*, *133*, 1443–1462.

Timmreck, C., and M. Schulz (2004), Significant dust simulation differences in nudged and climatological operation mode of the AGCM ECHAM, *J. Geophys. Res.*, *109*, D13202, doi:10.1029/2003JD004381.

Twomey, S. (1977), The influence of pollution on the shortwave albedo of clouds, *J. Atmos. Sci.*, *34*, 1149–1152.

van den Heever, S. C., G. G. Carrio, W. R. Cotton, P. J. DeMott, and A. J. Prenni (2006), Impacts of nucleating aerosol on Florida Storms. part I: Mesoscale Simulations, *J. Atmos. Sci.*, doi:10.1175/JAS3713.1.

Warner, J. (1968), A reduction in rainfall associated with smoke from sugarcane fires - An inadvertent weather modification?, *J. Appl. Meteorol.*, *2*, 247–251.

Weisman, M. L., and J. B. Klemp (1982), The dependence of numerically simulated convective storms on vertical wind shear and buoyancy, *Mon. Weather Rev.*, *110*, 504–520.

Whitby, K. T. (1978), The physical characteristics of sulfur aerosols, *Atmos. Environ.*, *12*, 135–159.

Wicker, L. J., and W. C. Skamarock (2002), Time-splitting methods for elastic models using forward time schemes, *Mon. Weather Rev.*, *130*, 2088–2097.

Wilhelmson, R. B., and J. B. Klemp (1978), A numerical study of storm splitting that leads to long lived storms, *J. Atmos. Sci.*, *35*, 1974–1986.

Xu, K. M. (1995), Partitioning mass, heat, and moisture budgets of explicitly simulated cumulus ensembles into convective and stratiform Components, *J. Atmos. Sci.*, *52*, 551–573.

Young, K. C. (1993), *Microphysical Processes in Clouds*, 427 pp., Oxford Univ. Press, New York.

Zhang, M. H., and J. L. Lin (1997), Constrained variational analysis of sounding data based on column-integrated budgets of mass, heat, moisture, and momentum: Approach and application to ARM measurement, *J. Atmos. Sci.*, *54*, 1503–1524.

Zhang, M. H., J. L. Lin, R. R. Cederwall, J. J. Yio, and S. C. Xie (2001), Objective analysis of ARM IOP data: Method and sensitivity, *Mon. Weather Rev.*, *129*, 295–311.

L. J. Donner and Y. Ming, Geophysical Fluid Dynamics Laboratory, Princeton University, 201 Forrestal Road, Princeton, NJ 08540-6649, USA.

S. S. Lee, Department of Atmospheric, Oceanic, and Space Sciences, University of Michigan, 2455 Hayward Street, Room 1215 SRB, Ann Arbor, MI 48109, USA. (seoungl@umich.edu)

V. T. J. Phillips, Department of Meteorology, University of Hawaii, Manoa, 2500 Campus Road, Honolulu, HI 96822, USA.